
A key change in outer space

—

Neutron star mergers as a
probe of modifications of
general relativity and physics
beyond the standard model

Bachelorarbeit

zur Erlangung des akademischen Grades
Bachelor of Science (B.Sc.) in Physik
am Institut für Theoretische Physik (ITP)
der Goethe-Universität Frankfurt am Main

vorgelegt von Yannik Schaper

Matrikelnr.: 6345947

Erstgutachterin: Prof. Dr. Laura Sagunski

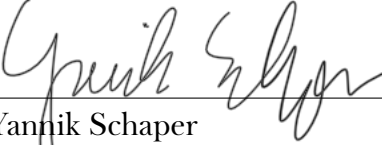
Zweitgutachter: Prof. Dr. Jürgen Schaffner-Bielich

eingereicht am 28. Nov. 2022

Selbstständigkeitserklärung

Hiermit erkläre ich, dass ich die Arbeit selbstständig und ohne Benutzung anderer als der angegebenen Quellen und Hilfsmittel verfasst habe. Alle Stellen der Arbeit, die wörtlich oder sinngemäß aus Veröffentlichungen oder aus anderen fremden Texten entnommen wurden, sind von mir als solche kenntlich gemacht worden. Ferner erkläre ich, dass die Arbeit nicht – auch nicht auszugsweise – für eine andere Prüfung verwendet wurde.

Eppstein, den 28. Nov. 2022



Yannik Schaper

Zusammenfassung

Diese Arbeit befasst sich mit einer Auswertung des Gravitationswellenereignisses GW170817 detektiert durch die LIGO und Virgo Observatorien. Anhand dieses Systems aus sich umkreisenden Neutronensternen sollen Abweichungen zu der Vorhersage der allgemeinen Relativitätstheorie, insbesondere eine schnellere Erhöhung der Frequenz in der Wellenform, gesucht werden. Sowohl Modifikationen dieser Theorie, als auch ein Effekt auf Grund der Anwesenheit von dunkler Materie stellen dafür mögliche Erklärungen dar. Für die Auswertung der Daten wird ein statistischer Rückschluss auf die Eigenschaften des Systems durchgeführt, welcher, auf Grund der Komplexität dieses Vorgangs, nur mittels numerischer Methoden bewerkstelligt werden kann und eines Hochleistungsrechners für das Ausführen von Monte-Carlo-Simulationen bedarf. Um sicherzustellen, dass diese Umsetzung zu belastbaren Ergebnissen führt, wurden diese mit den veröffentlichten Informationen über das Neutronensternsystem des LIGO Observatoriums abgeglichen, bevor zusätzliche Parameter eingeführt wurden. Dabei zeigte sich grundsätzlich eine Übereinstimmung mit den LIGO Analysen, die Simulationen müssen aber weiter optimiert werden, um belastbare Evidenz für oder gegen die Anwesenheit einer zusätzlichen Kraft zu liefern.

Abstract

In this work the GW170817 gravitational wave merger event from the LIGO/Virgo observatory is analyzed. The data of the binary neutron star system should be searched for differences to the predictions of general relativity: A faster increase in frequency of the system could give a hint to necessary modifications of the theory or the presence of light scalar dark matter particles. The analysis is done by a Bayesian inference. The complexity of this method only allows for a numerical approach with a representation of the mathematical operations by Markov chain Monte Carlo methods and still needs to be done on a supercomputer. To ensure for the validity of the results, these were first compared to the published information about the system by the LIGO cooperation, before additional parameters were introduced. This resulted in general in comparable parameters to the LIGO analysis, but to allow for the search for evidence of the presence of an additional force a further optimisation of the inferences has to be done.

Contents

	Page
1. Introduction	1
2. Theoretical framework	3
2.1. Gravitational waves	3
2.2. Creation of gravitational waves	6
2.3. Inspiral of compact objects	7
2.4. Post-Newtonian-formalism	8
2.5. Tidal deformability	11
3. Modifications of the neutron star system	12
3.1. Neutron star inspirals with scalar forces	12
3.2. $f(R)$ -gravity	14
3.3. Axion dark matter	15
4. Parameter Inferences	16
4.1. Bayesian inference	16
4.2. Markov chain Monte Carlo	17
4.3. The PyCBC & LALSuite packages	18
4.4. Code modifications	20
5. Computation	24
5.1. Cluster usage	24
5.2. Submission scripts	25
6. Conducted inferences	29
6.1. The GW170817 Event	29
6.2. Sampler evaluation	30
6.3. Axion search	34
7. Conclusion & outlook	35
A. Code structure	37
B. Submission scripts	38
C. Inference files	42

Acronyms & Abbreviations

ACL	auto-correlation length
ALP	axion-like particle
CP	charge conjugation and parity
Dir	directory
DM	dark matter
DOF	degrees of freedom
EOS	equation of state
EOM	equation of motion
FS	file system
GR	general relativity
GRB	gamma ray burst
GW	gravitational waves
LALSuite	LSC (LIGO Scientific Collaboration) Algorithm Library Suite
LIGO	Laser Interferometer Gravitational-Wave Observatory
MCMC	Markov chain Monte Carlo
NS	neutron star
PN	post-Newtonian
PQ	Peccei-Quinn
PyCBC	Python for Compact Binary Coalescence
SNR	signal-to-noise-ratio
SPA	stationary phase approximation
symlink	symbolic link
TD	tidal deformability
TT	transverse-traceless
QFT	quantum field theory
QCD	quantum chromo-dynamics

1. Introduction

When we contemplate the enormous revolution in our understanding of the universe that has come from electromagnetic astronomy over the four centuries since Galileo, we are led to wonder what revolution will come from gravitational astronomy, and from its multi-messenger partnerships, over the coming four centuries.

Nobel Lecture 2017
Kip S. Thorne, LIGO initiator
[1] Concl.]

With the first gravitational wave detection in 2015, shortly after the Advanced LIGO observatory started its first observation run, a completely new era of astronomy began. Since the beginning of mankind the (night) sky was watched to learn about what is out there in the cosmos. Although our observation techniques evolved massively, making it possible to gather information about very small and faint objects and going beyond the visual frequency range, we have always been limited by only having the information accessible from the electromagnetic radiation that reaches us. But with this detection we opened another channel of observation, starting the era of multi-messenger astronomy. [2]

Gravitational waves as phenomena of the theory of general relativity were predicted quite early after the theory's publication. But because of the weakness of the force of gravity the predicted effects from these waves were so small, that it was not seen as unlikely for them never to be found in real measurements. Though, in the 1970th with the Hulse-Taylor-pulsar a first system was found, where effects of this radiation play an important role. It is a binary of two neutron stars emitting a rhythmic radio signal based on their orbiting period. It was found that the decrease of this period fits very well to the energy-loss from gravitational waves emission, resulting in a decrease of their distance. [3] By that the Hulse-Taylor-pulsar observation was the first indirect evidence for the existence of gravitational waves.

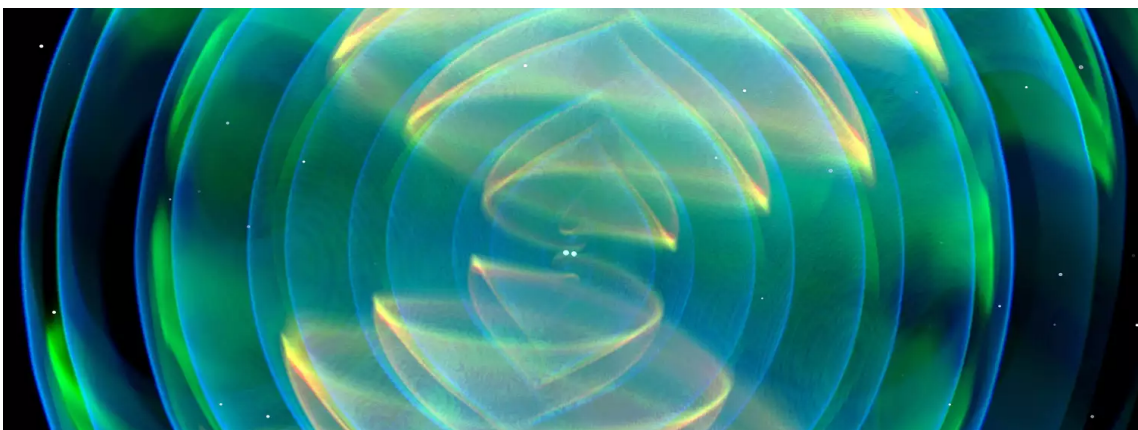


Figure 1: Artistic impression of the gravitational wave signal of a binary neutron star (reprinted from [4]).

With the LIGO and Virgo observatories direct observations became possible and until now several similar systems to the first one detected in 2015 were observed: Inspiring each other until colliding and merging into a new compact object. Figure 2 gives an overview of the detections, also showing that with the event from the 17th of August 2017 there is only one binary neutron star system observed by these (Information about the event including an auditory representations of the signal can be found at [5].), making this data very unique, until the upcoming observation run beginning in March 2023 hopefully will find more of its kind.

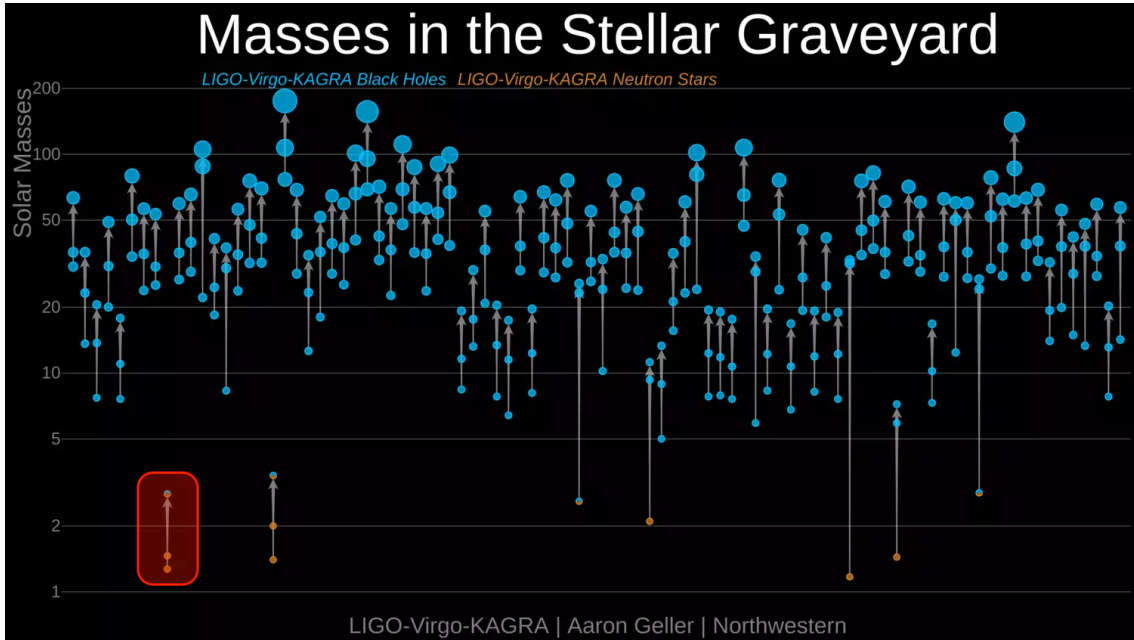


Figure 2: Initial and final masses of all observed gravitational wave detections with only one pure neutron star event GW170817 highlighted in red (modified and reprinted from [6]).

Neutron star binaries are of special interest, because as compact objects strong gravitational forces rule their dynamics. Although, gravity is still not strong enough for separating regions by an event horizon in these, which would drastically reduce the information that is send out. This would lead to a less complex system, but by that also a less capable cosmic laboratory. However one has to have in mind that in contrast to black holes their geometry is determined by their inner structure. For this the equation of state is still unknown, so ones results have to hold independent of its actual form. [7]

The goal of this work is to look for differences in the dynamics during the inspiral and by that to find a hint for a necessary modification of the theory of gravity or for effects of dark matter. Having neutron stars which are not only made of regular matter, but additionally are surrounded by a cloud of dark matter particles, will lead to an additional attracting force, when these start interacting. This will result in a modulation of the chirping signal, as if an upwards key change happens before the final orbits.

2. Theoretical framework

For this work the most important bedrock is the theory of general relativity (GR). It describes the dynamics of the observed compact objects like neutron stars, the structure of these themselves and even how we can receive the information about the systems via gravitational waves (GW). All this behaviour can be derived from its central part, the Einstein equations: $G_{\mu\nu} = 8\pi T_{\mu\nu}$.¹ They relate the curvature and by this the geometry of the universe via the metric of the spacetime contained in the Einstein tensor $G_{\mu\nu}$ to its content represented by the energy-momentum-tensor $T_{\mu\nu}$. A good overview of GR and its implications in Astronomy can be found in [8, ch. 17].

For this work, we will focus on GW and compact objects, before entering the realm of another fundamental theory: quantum field theory (QFT) for the description of dark matter (DM) as particles.

2.1. Gravitational waves

Considering the Einstein equations one has a set of second order differential equations. But it is not obvious that this will lead to a solution for radiation, as a simple wave equation like we know from electromagnetism ($\square A^\mu = 0$) would do. Looking for wave-like solutions [8, ch. 1.8] suggests considering spacetimes with small curvature represented by a line element which consists of a flat spacetime $\eta_{\mu\nu}$ plus a small deviation $h_{\mu\nu}$. This can be written as following:

$$g_{\mu\nu} = \eta_{\mu\nu} + h_{\mu\nu} + \mathcal{O}\left((h_{\mu\nu})^2\right), \quad |h_{\mu\nu}| \ll 1. \quad (1)$$

With this we ensure that all terms higher than linear order in $h_{\mu\nu}$ will also vanish in the derivatives of the metric and by that also in the Einstein tensor and similar ones. It becomes:

$$G_{\mu\nu} \equiv \bar{R}_{\mu\nu} = \left(\partial_{[\rho} \Gamma^{\rho}_{\mu]\nu}\right) = -\frac{1}{2} \left(\partial^\rho \partial_{[\rho} \bar{h}_{\mu]\nu} + \eta_{\mu\nu} \partial^\rho \partial^\tau \bar{h}_{\rho\tau}\right).^{2,3} \quad (2)$$

One part of the first term can be identified as the wanted D'Alembertian operator acting on the trace-free perturbation $\bar{h}_{\rho\tau}$. This is also the only non-vanishing term, if we use the gauge freedom inherent in GR. By the so called Lorenz gauge ($\partial_\rho \bar{h}_{\rho\nu} = 0$) the other terms are 0 and with the additional condition of $h_{\mu\nu}$ being traceless in the first place, $G_{\mu\nu}$ reduces to the right hand side of an ordinary wave equation. As a third condition one can set $T_{\mu\nu}$ to 0, which fits well to our assumption of an (besides GW contributions) flat spacetime in the beginning. Although this can only be true outside the source.

¹If not stated otherwise, in this work Planck's units are used, where $G = c = \hbar = 1$.

²Here the "bar-operator" is used as a short notation for trace-free tensors defined as $\bar{x}_{\mu\nu} := x_{\mu\nu} - 1/2 \eta_{\mu\nu} x^\rho{}_\rho$.

³In the index notation the square brackets describe the antisymmetrisation of the enclosed indices. For the simple case of two indices this is $x_{[\mu\nu]\rho} = 1/2(x_{\mu\nu\rho} - x_{\nu\mu\rho})$.

These three conditions (also stated in [8] ch. 1.8]), define the so-called transverse-traceless (TT) gauge. For this we finally get a wave equation

$$\square h_{\mu\nu}^{\text{TT}} = 0 . \quad (3)$$

Due to the gauge, 8 degrees of freedom (DOF) of $h_{\mu\nu}$ are fixed. So from the in general 10 linear independent components of a second order tensor only 2 DOF are left, with the result that the solution consists of two plane waves with different polarisation. They are referred to as plus "+" and cross "×". These names correspond to the distortion patterns they introduce interacting with free falling particles.

To see this another frame is needed. The so called proper detector frame has the property that the origin of the positions are defined by a rigid ruler and are not moving with the incoming GW like in the TT-frame. If we take a sufficiently small space region, it will be flat, even if GWs are present. Expanding this to second order it can be seen that, in opposite to the first order which vanishes by definition in a free falling frame at the expansion point, there are non-zero second order terms described by the Riemann tensor and

$$ds^2 = -dt^2 \left(1 + R_{0i0j} x^i x^j \right) - 2dt dx^i \left(\frac{2}{3} R_{0jik} x^j x^k \right) + dx^i dx^j \left(\delta_{ij} R_{ikjl} x^k x^l \right) . \quad (4)$$

For an earthbound detector there are additional terms due to the acceleration of earth's gravity g and angular velocity Ω . This can be found in an early paper by Kip Thorne [9] resulting in the metric

$$ds^2 = -dt^2 \left(1 + 2 \vec{g} \times \vec{x} + (\vec{g} \times \vec{x})^2 - (\vec{\Omega} \times \vec{x})^2 + R_{0i0j} x^i x^j \right) + 2dt dx^i \left(\varepsilon_{ijk} \Omega^j x^k - \frac{2}{3} R_{0jik} x^j x^k \right) + dx^i dx^j \left(\delta_{ij} R_{ikjl} x^k x^l \right) . \quad (5)$$

These additional terms especially the second order ones, which look like fictitious forces, have to be subtracted for separating the gravitational waves in the detector signal. Hereinafter it is assumed that these are changing much slower than the frequency of the gravitational waves and can be neglected.

From the geodesic equation in this frame taking two points with the distance ξ the deviation of this is given by the geodesic deviation equation:

$$\ddot{\xi}^i = -R^i{}_{0j0} \xi^j = \frac{1}{2} \ddot{h}_{ij}^{\text{TT}} \xi^j .^4 \quad (6)$$

Here one can see that the effect of the gravitational wave just looks like a Newtonian force between the two points. Assuming a wave propagation in x_3 -direction h_{ij}^{TT} can be written in its two polarisations

$$h_{ab}^{\text{TT}} = \left[h_+ \begin{pmatrix} 1 & 0 \\ 0 & -1 \end{pmatrix} + h_\times \begin{pmatrix} 0 & 1 \\ 1 & 0 \end{pmatrix} \right] \sin(\omega t) . \quad (7)$$

⁴Here it was used that in the TT-frame the Riemann tensor is directly related to the strain by $R_{i0j0} = -1/2 \ddot{h}_{ij}^{\text{TT}}$.

ωt	h_+	h_\times
0		
$\pi/2$		
π		
$3\pi/2$		

Figure 3: The deformation patterns for a ring of free-falling particles taken from [10], fig. 1.1].

By that (6) simplifies into a set of differential equations for two coupled harmonic oscillators for the modes. The corresponding patterns can be seen in figure 3.

The signal of a detector always consists of a mixture of these. The corresponding coefficients F in $h := F_+ h_+ + F_\times h_\times$ are called detector pattern functions. They depend on the angles between the detector plane and the propagation direction $\hat{N} := (\theta, \phi)$ (compare figure 4) as well as the angle between the x_0 -axis of the detector frame projected on the sky \hat{e}_x^R and the same of the coordinate system for the polarisation modes $\hat{\alpha}$ written as ψ . [11, ch. 4.2] The arrangement of these is depicted in figure 4 resulting in the definitions

$$\begin{aligned}
 F_+ &:= \frac{1}{2} [1 + \cos^2 \theta] \cos(2\phi) \cos(2\psi) - \cos \theta \sin(2\phi) \sin(2\psi), \\
 F_\times &:= \frac{1}{2} [1 + \cos^2 \theta] \cos(2\phi) \sin(2\psi) - \cos \theta \sin(2\phi) \cos(2\psi).
 \end{aligned}
 \tag{8}$$

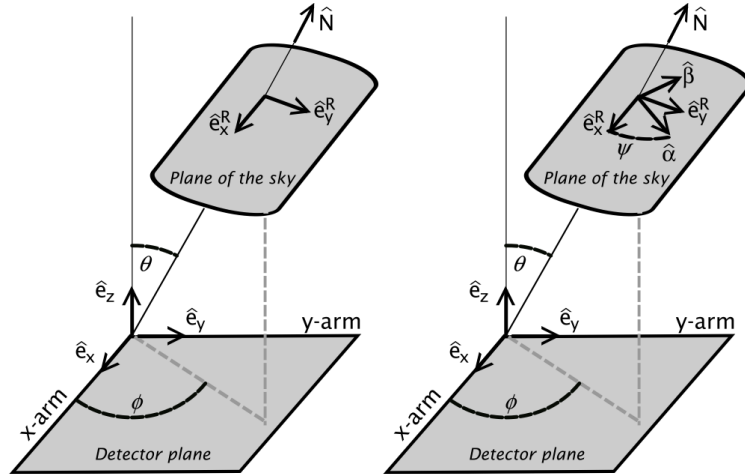


Figure 4: Sketch of the angles for the detector partition functions from the relative orientation of the sky frame taken from [11], fig. 3].

2.2. Creation of gravitational waves

The only question to be answered now before stating the existence of this gravitational radiation is, how these can be created. For this we have to allow for a non-zero energy-momentum tensor. This leads to following equation:

$$\square \bar{h}_{\mu\nu} = 16\pi T_{\mu\nu} . \quad (9)$$

Because this has the same form as the equations for the retarded potentials in electromagnetism, the solutions also will be analog to this [12, §110]: Integrating $T_{\mu\nu}$ retarded by the difference of time t and distance to the origin r over a volume which contains the whole source results in

$$\bar{h}_{\mu\nu} = -4 \int \frac{1}{R} (T_{\mu\nu})_{t-r} dV . \quad (10)$$

For slow velocities ($c \ll 1$) of all objects in the source their difference in position for waves leaving the volume at the same time will be negligibly small and the positions can be assumed as fixed. Additionally because of (9) the equations of the traceless gauge also have to hold for $T_{\mu\nu}$ and can be rewritten in integral form as

$$\int T_{ij} dV = \frac{1}{2} \partial_0^2 \int T_{00} x_\mu x_\nu dV . \quad (11)$$

With these two we can rewrite $h_{\rho\nu}$ as an integral only over the energy density component $\rho := T_{00}$. Although this definition only holds in the non-relativistic case. The expression then can be recast to include the quadrupole moment of the energy Q_{ij} in

$$\bar{h}_{ij} = -\frac{2}{r} \partial_0^2 \int \rho x_i x_j dV = -\frac{2}{r} \ddot{Q}_{ij} , \quad Q_{ij} := \int \rho \left(x_i x_j - \frac{r^2}{3} \delta_{ij} \right) dV .^5 \quad (12)$$

Picking the direction x_1 and assuming a position far away from the source the generated energy current will travel in the form of a plane wave on the flat background metric as described in section 2.1. By that it also gets a simpler form: Knowing \bar{h}_{ij} the component T_{01} can also be recast as a function of the quadrupole moment

$$T_{01} = \frac{1}{16\pi} \left[\dot{h}_{23}^2 + \frac{1}{4} (\dot{h}_{22} - \dot{h}_{33})^2 \right] = \frac{1}{4\pi r^2} \left[\ddot{Q}_{23}^2 + \frac{1}{4} (\ddot{Q}_{22} - \ddot{Q}_{33})^2 \right] . \quad (13)$$

For the total energy which is radiated away this only has to be integrated over the surface of the volume. For that the direction will be generalised by the unit vector n_i in direction of propagation. This leads to an average over all directions in the well known quadrupole formula

$$\dot{E} = - \int T_{0r} dA = - \int \frac{1}{r} \left[\ddot{Q}_{ij} \ddot{Q}_{ik} n_j n_k - \frac{1}{2} (\ddot{Q}_{ij} n_i n_j)^2 - \frac{1}{4} (\ddot{Q}_{ij})^2 \right] dr = -\frac{1}{5} \langle \ddot{Q}_{ij}^2 \rangle .^6 \quad (14)$$

⁵The dot-operator describes the derivative regarding time.

⁶For the average over all directions a relation for general quadrupole radiation was used. [12, §71]

2.3. Inspiral of compact objects

Writing the quadrupole formula in SI-units there is an additional factor of c^{-5} . By that the energy transmitted via GWs will be very small. So looking for GWs compact objects are a good choice, maximising the strength of the gravitational field. The other important part for generating GWs is having a changing quadrupole tensor. Because of that single compact objects are excluded as strong sources and we are looking into a system a bit more complex:

Starting with two compact objects orbiting each other and around the x_3 -axes, in the centre of mass frame the density distribution in polar coordinates is

$$\rho = \mu \delta(r - R) \delta(\phi - 2\omega_s t) \delta(\theta) . \quad (15)$$

Here $\mu := (1/m_1 + 1/m_2)^{-1}$ is the reduced mass, $R := r_1 - r_2$ the distance of the two objects and the angle in ϕ -direction is given using Kepler's law for the orbital frequency $\omega_s = \sqrt{M/R^3}$ with $M = m_1 + m_2$. [13, ch. 4.1] For this the orbit is assumed to be circular, which is true after a sufficient amount of energy has radiated away. Putting this into the definition of the quadrupole and then its derivative into the quadrupole formula, the radiated power is

$$\dot{E} = -\frac{32}{5} (M_c \omega_s)^{10/3} , \quad M_c := \mu^{3/5} M^{2/5} . \quad (16)$$

The introduced quantity M_c is the so-called chirp mass. It is leading to an important characteristic of the GW signal: Because of the emitted energy the orbital energy will decrease, the radius will get smaller as well and by that the frequency will increase. So the signal will have a chirp-like increase in the frequency as well as amplitude while the objects are inspiraling. But as long as $\dot{\omega}_s \ll \omega_s^2$, the orbits will be quasi-circular with only a slow change of R , which is not significant in the total velocity.

Because of that, we can derive the change of the frequency over the orbital energy E_{orb} for circular Keplerian motion by replacing the radius with Kepler's law in

$$E_{orb} = -\frac{m_1 m_2}{2R} = -\left(\frac{M_c^5 \omega_s^2}{8}\right)^{1/3} , \quad (17)$$

where in addition to that the definition of M_c was used.

From the conservation of energy we know that the derivative of this energy has to be equal to the energy emitted as GWs. So by setting these equal, one can get the derivative of ω_s or of the actual detected GW frequency $f_{gw} = \omega_s/\pi$:

$$\dot{f}_{gw} = \frac{96\pi^{8/3}}{5} M_c^{5/3} f_{gw}^{11/3} . \quad (18)$$

Because the solution of this differential equation diverges at finite times, it is natural to describe f_{gw} in terms of the difference of time to this event at coalescence t_c , which is called $\tau := t_c - t$. This results into

$$f_{gw} = \frac{1}{\pi} \left(\frac{256}{5} \tau \right)^{3/8} M_c^{-5/8}. \quad (19)$$

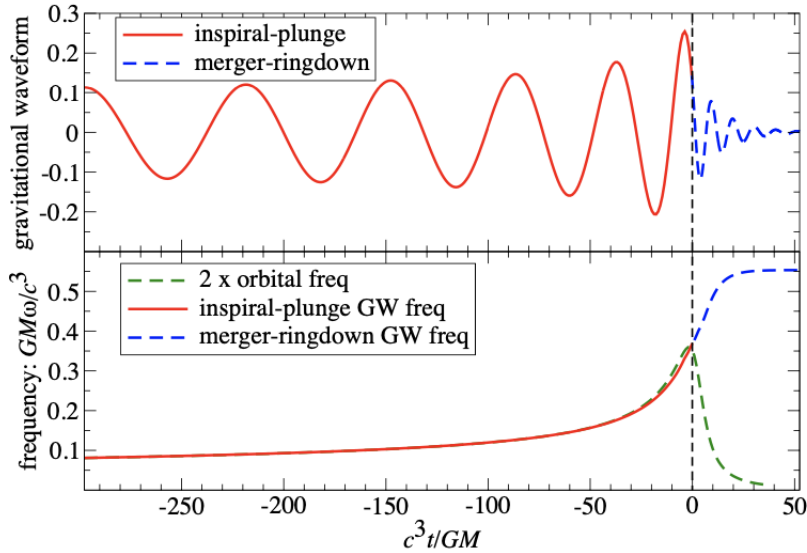


Figure 5: Example for the waveform and increasing orbital frequency until coalescence at $t = 0$ (reprint of [14, fig. 4]).

This can be seen in figure 5 together with the resulting waveform, which has as a result of the rising luminosity an increasing amplitude as well. In addition to that we can also compute the radius and its development over time using this frequency relation and (17):

$$R = \frac{m_1 m_2}{M_c^{5/3} \omega_s^{2/3}} = \left(\frac{256}{5} \mu M^2 \tau \right)^{1/4}. \quad (20)$$

2.4. Post-Newtonian-formalism

Until now we assumed the low velocity approximation of the quadrupole formula. But knowing that the orbital frequency will increase during the inspiral, this will break down at some point. To extend the solution to regions in which relativistic effects play an important role, we use perturbation theory in regards to the velocity. This is called post-Newtonian (PN)-formalism and the order until the expansion is done is called PN-order.

For this we introduce the dimensionless variables for the time coordinate and orbital frequency as stated in [13], ch. 5.6]:

$$\begin{aligned}\theta &:= \frac{\mu}{5M^2} \tau, \\ \xi &:= (M\omega_s)^{2/3} = \mathcal{O}(v^2).\end{aligned}\tag{21}$$

By that the corrections of order v can be expressed in powers of $\xi^{1/2}$. With these the Keplerian orbit can be described simply by inserting the radius-frequency-relation and (20) leading to

$$\begin{aligned}\xi &= \frac{M}{R} = \frac{1}{4} \theta^{-1/4}, \\ \phi &= \phi_0 - \frac{M}{\mu} \theta^{5/8} = \phi_0 - \frac{M}{32\mu} \xi^{-5/8}.\end{aligned}\tag{22}$$

For computing the waveform it is important to expand the expressions to high enough order. For example one can see from the frequency dependency of the phase of $f^{-5/3} \propto \xi^{-5/2}$ that for small frequencies corrections of these diverge or stay finite up to 2.5 PN, so at least all terms up to 3 PN should be kept. For the following derivation the 3.5 PN-order is used. For this one can find divergencies in some integrals due to the Dirac delta in the description of point-like particles, so there is the need for regularisations for this term.

The equation of motion (EOM) has the general form

$$\ddot{x}_i = -\frac{M}{R^2} \left[(1+A) \frac{x_i}{r} + B\dot{x}_i \right],\tag{23}$$

where A and B are very long expressions, which can be found in [15], ch. 9.3]. But for circularised orbits most of their terms can be dropped because of the vanishing radial velocity. To 3.5 PN-order the EOM becomes

$$\ddot{x}_i = -\omega_s^2 x_i - \zeta \dot{x}_i,\tag{24}$$

where

$$\begin{aligned}\omega_s &= \frac{\xi^3}{M^2} \left\{ 1 + (-3 + \nu) \xi + \left(6 + \frac{41}{4} \nu + \nu^2 \right) \xi^2 \right. \\ &\quad \left. + \left[-10 + \left(22 \log \left(\frac{r}{r_0} \right) - \frac{75707}{840} + \frac{41}{64} \pi^2 \right) \nu + \frac{19}{2} \nu^2 + \nu^3 \right] \xi^3 \right\}, \\ \zeta &= -\frac{32}{5} \frac{\nu \xi^4}{M}.\end{aligned}\tag{25}$$

Here the symmetric mass ratio $\nu := \mu/M$ was introduced as a dimensionless alternative to μ and r_0 appears as a gauge-dependent length-scale. This cancels out for physical observable quantities like the orbital energy

$$\begin{aligned}E_{orb} &= \frac{\nu M \xi}{2} \left\{ 1 + \left(-3 + \frac{1}{3} \nu \right) \frac{\xi}{4} + \left(-27 + 19\nu + \frac{1}{3} \nu^2 \right) \frac{\xi^2}{8} \right. \\ &\quad \left. + \left[675 + \left(\frac{34445}{9} + \frac{410}{3} \pi^2 \right) \nu + \frac{310}{3} \nu^2 + \frac{35}{81} \nu^3 \right] \frac{\xi^3}{64} \right\}.\end{aligned}\tag{26}$$

Using this together with the PN-expanded version of the energy flux⁷

$$\begin{aligned} \dot{E} = \frac{32\nu M \xi^5}{5} & \left\{ 1 + \left(-\frac{1247}{84} - \frac{35}{3}\nu \right) \frac{\xi}{4} + 4\pi \xi^{1.5} + \left(-\frac{44711}{1134} + \frac{9271}{63}\nu + \frac{260}{9}\nu^2 \right) \frac{\xi^2}{8} \right. \\ & - \left(\frac{8191}{672} + \frac{583}{24}\nu \right) \pi \xi^{2.5} + \left[\left(\frac{6643739519}{1091475} + \frac{1}{12}\pi^2 + \left(-\frac{269086}{243} + \frac{164}{3}\pi^2 \right) \nu \right. \right. \\ & \quad \left. \left. + \frac{377612}{189}\nu^2 + \frac{12400}{81}\nu^3 \right) \frac{1}{64} - \frac{1712}{105}\gamma - \frac{856}{105} \log(16\xi) \right] \xi^3 \\ & \left. + \left(-\frac{16285}{504} + \frac{214745}{1728}\nu + \frac{193385}{3024}\nu^2 \right) \pi \xi^{3.5} \right\} \end{aligned} \quad (27)$$

in the energy balance equation and solving these analog to section [2.3](#) leads to the solution *TaylorF2* [\[16\]](#), which uses the stationary phase approximation (SPA), for the orbital phase

$$\Psi(f) = 2\pi t_c f - \frac{\pi}{4} + \Psi_{3.5 \text{ PN}}^{(F2)} - \Psi_c \quad (28)$$

with t_c and the phase Ψ_c at this point in time set by boundary conditions. The term $\Psi_{3.5 \text{ PN}}^{(F2)}$ due to the PN-correction is defined as

$$\begin{aligned} \Psi_{3.5 \text{ PN}}^{(F2)} := \frac{3}{128\nu} \xi^{-2.5} & \left\{ 1 + \frac{20}{9} \left(\frac{743}{336} + \frac{11}{4}\nu \right) \xi - 16\pi \xi^{1.5} \right. \\ & + 10 \left(\frac{3058673}{1016064} + \frac{5429}{1008}\nu + \frac{617}{144}\nu^2 \right) \xi^2 \\ & + \left(\frac{38645}{756} + \frac{65}{9}\nu \right) \left[1 + 3 \log \left(\frac{\xi}{\xi_{lso}} \right) \right] \pi \xi^{2.5} \\ & + \left[\frac{11583231236531}{4694215680} - \frac{640}{3}\pi^2 - \frac{6848}{21} (\gamma + \log(4\xi^{0.5})) \right. \\ & \quad \left. + \left(-\frac{15737765635}{3048192} + \frac{2255}{12}\pi^2 \right) \nu + \frac{76055}{1728}\nu^2 + \frac{127825}{1296}\nu^3 \right] \xi^3 \\ & \left. + \left(\frac{77096675}{254016} + \frac{378515}{1512}\nu - \frac{74045}{756}\nu^2 \right) \pi \xi^{3.5} \right\}. \end{aligned} \quad (29)$$

⁷Here γ is the Euler-Mascheroni constant ($\gamma = 0.57721\dots$).

2.5. Tidal deformability

For a binary neutron star (NS) system there is an additional correction term for the phase. This Ψ_{TID} term comes from the fact that they are no perfect spheres and adds to the phase corrections from the PN expansion. In the lowest order it has the form

$$\Psi_{TID} = -\frac{9}{16} \frac{\xi^{2.5}}{\nu} \left[\left(1 + 12 \frac{m_2}{m_1}\right) \Lambda_1 + \left(1 + 12 \frac{m_1}{m_2}\right) \Lambda_2 \right], \quad (30)$$

where Λ_1 and Λ_2 ⁸ are the tidal deformabilities (TDs) of the NSs.

Because of this the TDs first appear in PN-order 5. But, because Ψ_{TID} is typically larger than the terms in the PN-expansion, it still plays an important role for the inspiral dynamics. By describing the deviation from the spherical shape of the NSs, when a force between these is present, they are a measure for how closely the system resembles two interacting point-like particles. It can be found that the TDs of NSs are very large [18], so the reaction to the tidal field is very small and this approximation is valid.

In general the TDs depend on the equation of state (EOS), for which there are many different models describing NSs, but if the two obey the same EOS, also their TDs are related. [19] Introducing the symmetric TD $\Lambda_s := 1/2 (\Lambda_1 + \Lambda_2)$, the antisymmetric TD $\Lambda_a := 1/2 (\Lambda_1 - \Lambda_2)$ and the mass ratio $q := m_1/m_2$ one can find an EOS-insensitive relation for Λ_a like stated in [20]:

$$\Lambda_a = F_n(q) \Lambda_s \frac{a + \sum_{i=1}^3 \sum_{j=1}^2 b_{ij} q^j \Lambda_s^{-i/5}}{a + \sum_{i=1}^3 \sum_{j=1}^2 c_{ij} q^j \Lambda_s^{-i/5}}, \quad F_n(q) := \frac{1 - q^{10/(3-n)}}{1 + q^{10/(3-n)}} \quad (31)$$

with the coefficients a , b_{ij} and c_{ij} given in table 1. Using this relation there is only Λ_s left as a free parameter in Ψ_{TID} .

a					
0.075 50					
b_{11}	b_{12}	b_{21}	b_{22}	b_{31}	b_{32}
-2.235	0.8474	10.45	-3.251	-15.70	13.61
c_{11}	c_{12}	c_{21}	c_{22}	c_{31}	c_{32}
-2.048	0.5976	7.941	0.5658	-7.360	-1.320

Table 1: Numerical coefficients for the TD-relation in (31) taken from [20, tab. 1].

⁸These are defined as the ratio of an external tidal field and the resulting quadrupole moment of the object calculated to linear order. They are related to the so-called tidal Love numbers by $\Lambda = \xi^{-5} k_2$. [17]

3. Modifications of the neutron star system

Until now we assumed that the only present force regarding the inspiral dynamics is gravity. Introducing another force we can alter the dynamics significantly, as long as this fifth force has a different dependency on the distance of the NSs. [21] This force is mediated by a scalar field and it will be shown, how modifications of gravity as well as the presence of particle DM can result in equivalent dynamics to the presence of a scalar field.

3.1. Neutron star inspirals with scalar forces

The NSs are again treated as point-like objects, but with an additional scalar field and for that a mass m_i and a charge q_i are assigned to them. With this, in a scenario where the corresponding massive scalar field ϕ with potential V is linearly coupled to the trace of the energy momentum tensor T , the action neglecting gravity like stated in [22, ch. II] is

$$S = - \int \left[\frac{\partial \phi^2}{2} + V - \beta \phi T \right] d^4x . \quad (32)$$

In this the parameter β is dimensionless and describes the strength of the coupling to the field. Neglecting relativistic effects T reduces to just the matter density ρ . If we now also assume a static scalar density field $\phi_0(r)$ with the mass m_s the EOM is

$$\phi_0'' + \frac{2}{r} \phi_0' = m_s^2 \phi_0 + \beta \rho . \quad (33)$$

Solving this second order differential equation one can simply use a Green's function and the assumption of a point-like object⁹ from the beginning:

$$\phi_0(r) = \beta \int \frac{e^{-m_s(r-\tilde{r})}}{|r-\tilde{r}|} \rho(\tilde{r}) d\tilde{r} = \beta \frac{e^{-m_s r}}{r} m_i + \phi_\infty . \quad (34)$$

Taking now the situation of two NSs with the field of one inducing a force on the other one, this force is

$$F_\phi = \beta M_2 \nabla \phi = \beta^2 m_1 m_2 \nabla \left(\frac{e^{-m_s r}}{r} \right) = q_1 q_2 m_1 m_2 \nabla \left(\frac{e^{-m_s r}}{r} \right) , \quad (35)$$

where for the last step a potential energy V_ϕ was defined in analogy to gravity. This has the form of a Yukawa-type potential:

$$V_\phi := -q_1 m_1 \frac{e^{-m_s r}}{r} . \quad (36)$$

⁹The point-like nature is described by the Dirac distribution and $\rho(r) := M_i \delta(r)$.

A connection between the charges and coupling strength β can be established, if $m_1 = m_2 \equiv m$ and $q_1 = q_2 \equiv q$. In this case one can read from (35) that $q = \sqrt{2} \beta$, which can even be done, if one only assumes the NSs to be constant density spheres with a radius r_c . For this case [22, ch. II] shows that

$$q^2 = \begin{cases} 2\beta^2 & \text{if } \frac{\Delta r_c}{r_c} > 1 \\ 2\beta^2 \left(\frac{3\Delta r_c}{r_c} \right) & \text{if } \frac{\Delta r_c}{r_c} \ll 1 \end{cases}, \quad \frac{\Delta r_c}{r_c} = (\phi_\infty - \phi_c) \frac{r_c}{6\beta M}, \quad (37)$$

where the first case is the expected result equal to a point charge. For this work we will focus on systems where this is the case and $\frac{\Delta r_c}{r_c}$ is small.

If we now describe the dynamics of an inspiral as discussed in section 2.3 having the distance R , (35) leads to

$$|F_s| = \frac{q_1 q_2 m_1 m_2}{R^2} (1 + m_s R) e^{-m_s R} \quad (38)$$

for the magnitude of the attractive force between the NSs.

Because the range of the force is determined by the Compton wavelength $\lambda := 1/m_s$, it is expected that this force starts to play a significant role in the final stages of the inspiral, where the orbit has circularised. So for the orbital frequency ω_s we can take the Keplerian relation also used in section 2.3 and modify it for the additional centrifugal force, so it gets

$$\omega_s^2 = \frac{M}{R^2} A, \quad A(q_1, q_2, m_s R) := 1 + q_1 q_2 (1 + m_s R) e^{-m_s R}. \quad (39)$$

Also for the change of the orbital frequency (18) has to be modified. For this we take a version of (17) where the additional force is added and differentiate it resulting in

$$\dot{E}_{orb} = \frac{d}{dt} \left[- \left(\frac{M_c^5 \omega_s^2}{8} \right)^{1/3} \right] = B(q_1, q_2, m_s R) \mu R \omega_s \dot{\omega}_s. \quad (40)$$

In this the dimensionless coefficient b was defined as

$$B(q_1, q_2, m_s R) := 1 - \frac{4A}{3 + q_1 q_2 (3 + 3m_s R + m_s^2 R^2) e^{-m_s R}}. \quad (41)$$

Then also the additional loss of energy due to scalar radiation has to be taken into account. This is in contrast to the GW radiation related to the dipole moment for its lowest term. By that the frequency will be the same as the orbital frequency and the emitted power is

$$\dot{E}_s = \frac{[\mu R (q_1 - q_2) \omega_s^2]^2}{6}. \quad (42)$$

Having both sources of energy loss – the gravitational radiation in (16) and scalar radiation in (42) – one can again use the balance equation to get an expression for the change of the orbital frequency and by that also of the frequency of the GW

$$\dot{f}_{gw} = \frac{A^{2/3}}{-3B} \frac{96\pi^{8/3}}{5} M_c^{5/3} f_{gw}^{11/3}. \quad (43)$$

This shows that, because by definition $A > 1$ and $B \in (1, 1/3)$, the frequency increase will be higher than in the GR case and also the frequency at coalescence will be higher due to the additional force and faster orbital frequency.

Generally speaking an analytic expression for the frequency and the phase can not be obtained. But simulation results of these for different masses can be found in [22, fig. 1&2], an example for the modification of the strain of the GW is calculated in [23] and in the limit, where the scalar mass goes to 0, there is the expression

$$\Psi(f) = 2\pi t_c f - \frac{\pi}{4} + \frac{3}{4(1 + \alpha^2)^{2/3}} (8\pi M_c f)^{-5/3} - \Psi_c, \quad (44)$$

where Ψ_c is an integration constant defined by the phase at time of coalescence.

3.2. $f(R)$ -gravity

A simple modification to GR can be done by generalising the Einstein-Hilbert action and, instead of the Ricci scalar R itself, allowing for arbitrary functions of it by

$$S \propto \int \sqrt{-g} f(R) d^4x + S^M. \quad (45)$$

It can be shown that this is dynamically equivalent to GR with a scalar field $\phi \propto \ln f'(R)$ [24] and the action

$$\tilde{S} \propto \int \sqrt{-\tilde{g}} \left[\tilde{R} - \frac{1}{2} \partial_\mu \phi \partial^\mu \phi - V_\phi \right] d^4x + \tilde{S}^M. \quad (46)$$

This class of theories is very interesting because it can be used to model inflation as well as the current accelerated expansion of the universe with a scalar field [25] and also viable dark matter candidates.

For this work it is assumed that $f(R)$ is of the form $f(R) = R + a_2 R^2$, where there is only one additional parameter a_2 resulting in the potential

$$V_\phi \propto m_\phi^2 \left(1 - e^{-\beta\phi} \right)^2, \quad m_\phi := \frac{\beta}{\sqrt{a_2}}. \quad (47)$$

It can be shown that in this case stable solutions for NSs can be constructed (modified mass radius relations and equations of state can be found in [26]). For these the coupling β has the strength $\beta = 1/\sqrt{6}$ and as expected also in the picture of a scalar field there is only one free parameter. [22, ch. III]

¹⁰In GR g is the determinant of the metric tensor $g_{\mu\nu}$.

3.3. Axion dark matter

For DM there are many possibilities to construct viable candidates. Assuming that it is described by fundamental particles well studied candidates are axions. These are very light bosons with only a weak coupling to regular matter. [27, ch. 2]

They were originally postulated as a result of a spontaneous symmetry breaking in the Peccei-Quinn (PQ)-mechanism. This is a solution to the charge conjugation and parity (CP)-problem, which means that the standard model of particle physics or to be more precise the structure of the strong nuclear force¹¹ permits a combined breaking of the symmetry in these two quantities.

But strong CP-violating interactions inside the neutron would result in it having a large electric dipole moment, which is contradicting experimental constraints. By that the violating term has to be very small, which is in contrast to the assumption of the "naturalness" of parameters in the standard model. This is solved by adding the so-called PQ-symmetry, which promotes the term to an individual field with its own dynamics.

The result is an effective potential of periodic nature in which corresponding particles, the axions are oscillations around the minima of this. To generate a population of axions in today's universe its decay rate has to be very small¹², so that after the decoupling at a given temperature in the early universe the population does not dissipate resulting in a pressure-less axion gas. Because the small decay rate also suppresses the interaction with other matter, it is almost non-interacting and can contribute to DM.

For axions as DM candidates there also are several models, which go beyond the so-called quantum chromo-dynamics (QCD)-axion described above. These axion-like particles (ALPs) have masses and decay constants as independent parameters, so models typically can be characterised by the ALP mass plus the type of coupling to regular matter and the coupling strength linked to the decay constant. For the mass there is only a weak constraint, that it has to be between 1×10^{-2} and 1×10^{-22} eV [30, fig. 6].

¹¹The reason for this is the QCD vacuum structure, which has to be compatible with the axial U(1)-symmetry of this theory. More regarding this topic can be found in [28].

¹²In an early paper of Preskill and Wilczek it was found that the decay rate has to be at maximum of the order of 1×10^{12} GeV [29].

4. Parameter Inferences

Until now this was a description of how the GW signal will look like for a given system. In the case of a real observation though, we are facing the inverse problem. From the detected signal as much information as possible should be found regarding its source. This will be much more difficult and cannot be done in the same analytic manner. In the following will be described, how we can numerically reconstruct the parameters of the source in a way, which allows us to also use additional prior information. It is a probabilistic method, so its results will be a whole distribution of the likelihood of parameter values instead of a single value.

4.1. Bayesian inference

As a starting point for the inference we take Bayes theorem for conditional probabilities as described in [31, ch. 3.1]. Noting the event of receiving the given data d and the description via a given parameter set θ the probability for these parameters describing the given data or short posterior is given by

$$P(\theta|d) = \frac{P(d|\theta)}{P(d)} P(\theta) . \quad (48)$$

The probability $P(\theta)$ without the condition of describing the concrete data set is called prior, because it describes the belief in the parameter values before knowing the data set. In the fraction $P(d|\theta)$ is the *likelihood* or probability of receiving this data given the parameter set and a normalising constant in the denominator called *evidence*. This can be calculated integrating the likelihood over the whole parameter space. Often this is not calculated and the posterior is given up to a constant factor.

We first take a closer look at the prior. It is not given by the theory and has to be selected appropriately. In the end the posterior should converge to an objective result even if starting from different priors. But one important property is, that if the prior is 0 for a value the posterior also can only be 0 there, like it can easily be seen from (48). So it is important to ensure a non-zero prior in the whole expected parameter space. This leads to a simple choice as a uniform prior on θ , which can be defined like in [31, eq. 73]:

$$P(\theta) := \begin{cases} (\theta_l - \theta_h)^{-1} & \text{for } \theta \in [\theta_l, \theta_h] \\ 0 & \text{otherwise} \end{cases} , \quad (49)$$

where θ_l and θ_h are the upper and lower boundary of the possible parameter space.

This can be done similarly for higher dimensional parameter sets. But it is important to have in mind, that for high dimensional spaces this choice is far from being equal for all possible values. Practically when having an n -dimensional hypercube most of its volume is close to its surface and corners as it is derived in [32, ch. 7]. Because for continuous parameters there is no alternative without the same or similar issues, for the following data analysis uniform priors will be used for all parameters or a combination of parameters.

For the posterior being a high dimensional distribution the important part is converting it to a form which will be better accessible. This can be done by integrating over most of the parameters until only a one- or two-dimensional posterior for these parameters is left. This is called marginalisation. If we call the parameters to be excluded for this evaluation ψ and the parameter we are interested in ϕ , this looks like

$$P(\phi|d) \propto \int P(\phi, \psi|\theta) P(\phi, \psi) d^n \psi . \quad (50)$$

The only part left is the likelihood. Because this has to do with how the data is obtained, it should reflect the possible errors for this. A normal distribution is a good option representing Gaussian noise in the observation process, but also nuisance parameters regarding the measurement play a role. Because this is specific to the observation, the concrete form of the likelihood will be described with more details in the section [4.3](#).

4.2. Markov chain Monte Carlo

Markov chains are defined as sequences, where the $(n + 1)$ -th element only depends on the n -th element (more details can be found in [\[31\]](#) ch. 3.6). They are a useful tool, because they converge to a certain stationary state, for which there is no n -dependence when taking a large enough sample set. If we now take a chain of random variables with some kind of distribution, the chain will be a sample of this target distribution after an initial phase. The characteristic quantity for it is the transition probability, which describes the probabilistic nature of the generation of the next link.

Taking our case of the posterior for the step from the point θ_i to $\theta_{(i+1)}$ the transition probability $T(\theta_i, \theta_{(i+1)})$ is given by the detailed balance condition, which ensures the independence criterium

$$P(\theta_i|d) T(\theta_i, \theta_{(i+1)}) = P(\theta_{(i+1)}|d) T(\theta_{(i+1)}, \theta_i) , \quad (51)$$

which reflects that taking the ratio the transition probabilities it is inverse proportional to the posterior probability ratio.

With this sample the integrals mentioned in [4.1](#) can be approximated very easily. For the mean for example one gets with an N -elements long chain the expression

$$\langle \theta \rangle := \int \theta P(\theta_i|d) d\theta \approx \frac{1}{N} \sum_{i=0}^{N-1} \theta_i , \quad (52)$$

which also holds, if one replaces θ with any function of it or for multidimensional integrals. So the marginalisation in [\(50\)](#) can be conducted by dividing the full range of the parameter space in the dimensions which should not be integrated out into bins and evaluate the amount of points in each of these.

The last thing to solve now is the practical generation of the chain. A simple way to replicate the transition probabilities is to start from a random point in parameter space, find a candidate for the next point nearby – for example by taking a Gaussian distribution as a *proposal condition* $q(\theta_0, \theta_c)$ around the original point and randomly choosing a point from this – and evaluate the posterior p_c at this point and then accept the candidate with the probability

$$\alpha = \min \left(\frac{p_c q(\theta_c, \theta_0)}{p_0 q(\theta_0, \theta_c)}, 1 \right). \quad (53)$$

If the proposal distribution is symmetric in its arguments the formula for α is even simpler, because the terms from this distribution cancel out. There the acceptance procedure can be done by choosing a random positive number smaller than 1 and accept the candidate, if this number is larger than α . An algorithm like this is called Metropolis-Hastings algorithm, it can be shown that it fulfils the detailed balance equation (51). [31, ch. 3.6.2]

This shows that Markov chain Monte Carlo (MCMC) methods can be a very useful tool solving the high-dimensional integrals to be dealt with in the inference process. But there are certain things to consider for ensuring a good enough representation of the posterior¹³:

- All points of the sample have to be from the converged phase. So parts of the chain from an initial phase have to be discarded. Also after that it is important to ensure that the exploration of the parameter space is sufficient. MCMC is a local algorithm which could be trapped around a local maximum. Trying different sampler algorithms can be a way to be certain that this is not the case.
- Successive points will have a certain degree of correlation. To obtain truly independent points one should use thinning, which means that only each k -th element will be used. A good result of this process will be indicated by a low auto-correlation of the thinned chain.

4.3. The PyCBC & LALSuite packages

To conduct the inferences Python for Compact Binary Coalescence (PyCBC) [33] is used. It is a python package of the Laser Interferometer Gravitational-Wave Observatory (LIGO)/Virgo cooperation "to explore astrophysical sources of gravitational waves" [34] and has many modules for all tasks which have to be performed running a GW-observatory. The focus for this work will be on the *PyCBC Inference* sub-package.

This will in principle conduct the inferences like stated in (49), but also uses input from physical models like for the waveform, depending on the parameters discussed in section 2 like chirp mass, spin or TD. [35, ch. 2.1] This is complicated by degeneracies for example of mass ratio and spins, which than may be broken again by another parameter. To get the best possible result, not the whole parameter space is used, but there are several physically motivated assumptions made, like that the binary will have a negligible eccentricity when reaching the detector bandwidth, and also the option to reduce the dimensionality further by allowing additional constrains like one gets from a electromagnetic counterpart.

¹³These can also be found in [31, ch. 3.7].

For different system a variety of waveform models are available, but we will focus on *TaylorF2*, which is tailored towards the description of NSs and has as one of its core features the implementation of the TD, which allows for the inclusion of effects of an additional force.

With that the likelihood function can be created assuming static Gaussian noise. [35, ch 2.2] In the next step the sampling is realised by supporting different samplers like *emcee* or *emcee_pt* [36]. These are ensemble samplers, which means that several chains are used in parallel to enhance their robustness. The individual chains are Metropolis algorithms like described in 4.2. The special part for *emcee_pt* is that it uses different "temperatures", which is an analogy coming from Hamiltonian based transition probabilities. By that the different chains are more freely moving, swapping positions regarding an additional acceptance criteria. This can help exploring separated modes in parameter space [37]. The *emcee* sampler performs the same sampling, but with a fixed temperature.

For the final result the chains are thinned and the burn-in phase is discarded. This can be done with the *max_posterior* test, which is true, if enough samples are close to the maximum of the posterior distribution. There is also the *nacl* test, which looks for the auto-correlation length (ACL) of the second half of the chains, which are declared as burned-in if the ACL is small in comparison to their length. In addition to the in (50) described calculation of the means, credible intervals are calculated for each parameter as well as each set of two parameters. This leads to the characteristic scatterplots, that can be seen for an example with four almost Gaussian distributed parameters in figure 6.

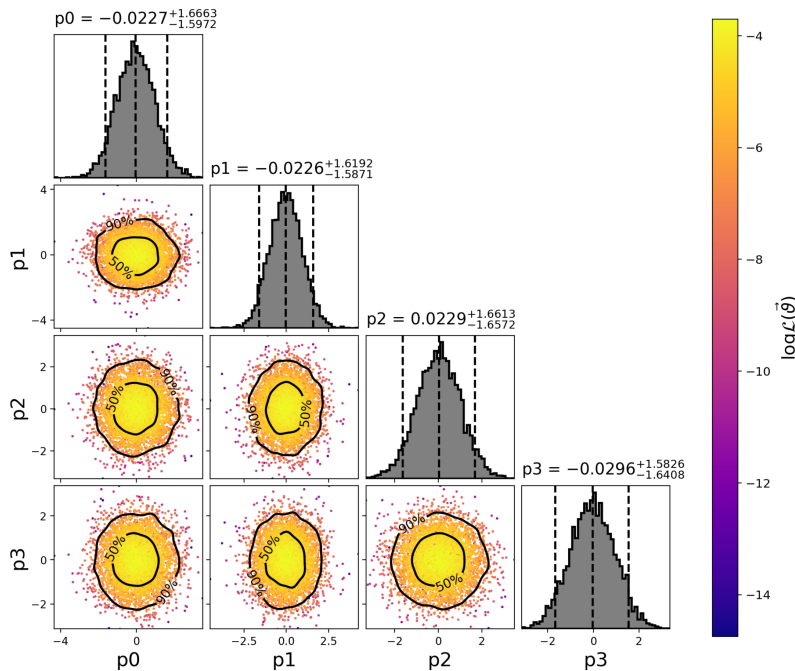


Figure 6: Example plot of the results of the *pycbc_inference* executable for the posterior of four parameters marginalised for all one- and two-dimensional combinations (reprint of [35, fig. 1]).

To conduct the inference an `pycbc_inference` called executable is provided. In the attached figure [14] its call graph is shown. For the user the most important objects are from the *Sampler*, *Transform* and *Distribution* classes, which can be manipulated by configuration files:

- The first kind, the *Sampler* objects, act as an interface to the external sampler packages and have to get handed the positions and posterior probabilities before performing a certain amount of steps and giving back the updated positions and posteriors. [35, ch. 3.2]
- The *Transform* objects in general only transform between coordinate systems. They make it possible to use a set of parameters which minimises their correlations for the sampling instead of the set requested by the user. This should lead to a faster convergence. [35, ch. 3.3] A good example for this is the chirp mass M_c instead of the individual masses of the two objects.
- The last ones, the *Distribution* objects are holding functions for the possible prior distributions. Here the general properties of the parameters and its constraints are entering.

Besides the sampling, the bulk of the underlying calculation is done with the LSC (LIGO Scientific Collaboration) Algorithm Library Suite (LALSuite) [38]. This includes different GW analysis routines written in C99, which can interface with PyCBC over SWIG [39] an interface compiler to generate wrapper around C/C++ libraries for interpreted languages like Perl, Ruby or here Python. This drastically increases the speed of the computation, while still allowing the user to interact with a more friendly python interface. Important for this work are the *Inspiral* routine which provides the waveform calculation and the *Inference* routine performing different tasks for the general inference process.

4.4. Code modifications

To make the inference of an additional parameter for the axion charge (like described in [3.1]) possible, a fork of the above mentioned packages was created. In the modified version of LALSuite (to be found on github at [40]) the central change was, that the *TaylorF2* waveform template was adjusted with an addition of a phase term in the *phasing* variable. Like shown in listing [1] this *axionPhi* is defined in lines 489 to 540 of `lalsimulation/lib/LALSimInspiralTaylorF2.c` for the case of an massive as well as massless axion. This has the reason that for a massive particle the effect should be only considered if the $v\beta$ called separation is below the Compton wavelength of it, which is checked for in line 506.

```

489 REAL8 axionPhi=0.;      /* the phase shift we want to compute */
490
491 if (axionlambda > 0.) { /* if lambda>0, massive axion*/
492     REAL8 axionalpha = 1./axionlambda; /* to ease readability and \\
        let the equations look like \\
        https://arxiv.org/pdf/2105.13963.pdf */
493     REAL8 v16=v12*v4, v18=v12*v6, v21=v18*v3;
494
495     gsl_sf_result resulterf;
496     gsl_sf_erf_e(sqrt(axionalpha)/v, &resulterf);
497

```

```

498 REAL8 pexpC = -5./8.*axionq/(v5*eta) * (exp(-axionalpha/v2)
499 * (4 + 32*v2/axionalpha + 138*v4/pow(axionalpha,2) + \
500 360*v6/pow(axionalpha,3) )
501 + 21*sqrt(LAL_PI)*v5*resulterf.val/pow(axionalpha,5./2.)
502 - 360*(1 - exp(-axionalpha/v2))*v8/pow(axionalpha,4));
503 /* these terms had to be separated, because for large \
alpha/v2 exp(+alpha/v2) was inf/0 and multiplying them \
gave nan */
504
505 if (v3 < axionalpha){
506 REAL8 p110AlphaC = \
0.0009682403233*pow(axiondq,2)*(3.621995839755853*v3 - \
6.889289848*axionalpha)
507 /(eta*pow(axionalpha,10./3.));
508
509 axionPhi = p110AlphaC + pexpC;
510 //printf("p110AlphaC = %e, ", p110AlphaC)
511 } else {
512 REAL8 consthyp = pow(axionalpha,2)/v6;
513
514 gsl_sf_result result1, result2, result3;
515 gsl_sf_hyperg_2F1_e(-5./6., 1./2., 1./6., consthyp, &result1);
516 gsl_sf_hyperg_2F1_e(-1./2., -1./3., 2./3., consthyp, &result2);
517 gsl_sf_hyperg_2F1_e(-1./3., 1./2., 2./3., consthyp, &result3);
518
519 REAL8 p110C = 5*pow(axiondq,2)/(2.54951424e8*v16*eta)*( -( \
520 sqrt(v6 - pow(axionalpha,2))*(-822640*pow(axionalpha,2)
521 + 227089*v18/pow(axionalpha,4) + \
261342*v12/pow(axionalpha,2) + 671304*v6 ))
522 + 140049*v21/pow(axionalpha,4)*result1.val
523 + 320*v3*result2.val*(1183*pow(axionalpha,2) - 741*v6 - \
684*v12/pow(axionalpha,2) + \
512*v18/pow(axionalpha,4))
524 + 960*v3*result3.val*(-1183*pow(axionalpha,2) + 741*v6 + \
684*v12/pow(axionalpha,2) - 80*v18/pow(axionalpha,4)));
525
526 axionPhi = p110C + pexpC;
527 //printf("p110C = %e, ", p110C);
528 }
529 } else { /* in the massless case */
530 /* m_sec=GM/c^3 total mass in seconds; piM = LAL_PI * m_sec;*/
531 /* massless axion, lambda->infinity */
532 REAL8 const1 = -0.125 * axionq/eta;
533 REAL8 const2 = - 5./896 * axiondq*axiondq/eta;
534 REAL8 const3 = 80./3. * axionq*axionp/eta;
535
536 /* v = cbrt(piM*f); massless axion */
537 axionPhi = const1*pow(v,-5) + const2*pow(v,-7) + const3*pow(v,-3);
538
539 }
540 }

```

Listing 1: Definition of *axionPhi* in *lalsimulation/lib/LALSimInspiralTaylorF2.c* from [40].

To allow for the additional four axion parameters *axionlambda*, *axionq*, *axionq1* and *axionq2* there are also additions to the *TaylorF2* file, the *lalsimulation/lib/LALSimInspiralWaveformParams.c* file and its corresponding header file.

In a fork of the PyCBC package in [41] this is also taken into account by adding lines for these parameters in *pycbc/waveform/waveform.py* (lines 174 – 185) and *pycbc/waveform/parameters.py*. In this lines 538 to 549 define objects for these before a list of them is added to the GR parameters in line 593.

Here the most significant difference is the definition of the *_Ls2lam_dq* function in the *pycbc/inference/models/gaussian_noise.py* file (lines 823 - 890 in listing 2) for the likelihood function. It calculates the TD from the masses and axion mass like described in (31) and exchanges its result with the standard values *lambda1* and *lambda2* in the *params* object.

```

823 def _Ls2lam_dq(params):
824     """
825     Calculates tidal deformability Lambda1, Lambda2 from the mass ratio
826     Values taken from https://arxiv.org/pdf/1804.03221.pdf
827     """
828     b = np.matrix([[ -27.7408,  8.42358], [122.686, -19.7551], \
829                  [ -175.496, 133.708]])
830     c = np.matrix([[ -25.5593,  5.58527], [92.0337, 26.8586], \
831                  [ -70.247, -56.3076]])
832     a = np.array([0.36, -0.0355, 0.000705])
833     mus = np.array([137.1252739, -32.8026613, 0.5168637, \
834                  [-11.2765281, 14.9499544, -4.6638851])
835     sigs= np.array([-0.0000739, 0.0103778, 0.4581717, -0.8341913, \
836                  [-201.4323962, 273.9268276, -71.2342246])
837     n = 0.743
838
839     #print("self.current_params:", self.current_params)
840     m1 = params['mass1']
841     m2 = params['mass2']
842     Ls = params['tidal_ls']
843     axion_q = params['axion_q']
844     qflip = m2/m1
845
846     Fnpow = qflip**(10./(3.-n))
847     Fn = (1. - Fnpow)/(1. + Fnpow)
848
849     # See eq (1) of https://arxiv.org/pdf/1804.03221.pdf
850     Ls_i = np.matrix([Ls**(-i/5.) for i in range(1,4)])
851     q_j = np.matrix([[qflip**j] for j in range(1,3)])
852     La = Fn* Ls * (1. + Ls_i*b*q_j) / (1. + Ls_i*c*q_j)
853     La = La[0,0]
854
855     # See eq (4)-(10) of https://arxiv.org/pdf/1804.03221.pdf
856     mu_ls = mus[0]/Ls/Ls + mus[1]/Ls + mus[2]
857     mu_q = mus[3]*qflip*qflip + mus[4]*qflip + mus[5]
858     mu_lsq = (mu_ls+mu_q)/2.

```

```

855
856 sig_ls = sigs[0]*Ls**(3./2.) + sigs[1]*Ls + sigs[2]*Ls**(1./2) + \\  

      sigs[3]
857 sig_q = sigs[4]*qflip*qflip + sigs[5]*qflip + sigs[6]
858 sig_lsq = np.sqrt(sig_ls**2 + sig_q**2)
859 La += np.random.normal(mu_lsq, sig_lsq)
860
861
862 lam1 = Ls - La
863 lam2 = Ls + La
864
865 if lam1<0 or lam1>lam2: # TODO: Check rate of occurrence
866     lam1=lam2=1.
867     C1=C2=1.
868     axion_q = 1.
869 else:
870     # See eq (78) of https://arxiv.org/pdf/1608.02582.pdf
871     C1 = a[0] + a[1]*np.log(lam1) + a[2]*np.log(lam1)**2
872     C2 = a[0] + a[1]*np.log(lam2) + a[2]*np.log(lam2)**2
873
874 # TODO: check significance of unused parameters
875 #signq = np.sign(axion_q)
876 #axiongamma = qflip * signq*C2/(C1*qflip) # qflip * \\  

      signq*(m1/C1)/(m2/C2)
877 #axion_gamma = signq * C2/C1
878 #axion_dq = np.sqrt(axionq/axion_gamma)*(1-axion_gamma)
879
880 params.update(tidal_ls=0) # not used in wf genertation
881 params.update(lambda1=lam1)
882 params.update(lambda2=lam2)
883
884 # see below eq(13) of https://arxiv.org/pdf/2105.13963.pdf
885 # TODO: check significance of m_a=0 condition
886 axion_p = (m1/C1+m2/C2)/(16.0*(m1+m2))
887 params.update(axion_p=axion_p)
888
889 #print('params:', params)
890 return params

```

Listing 2: Definition of the `_Ls2lam_dq` function calculating the TDs in `pycbc/inference/models/gaussian_noise.py` from [41].

To ensure that the forked versions are working as they were when they were created, an additional environment file `common/conda/preciseEnvironment.yml` was created with exact versions of all dependencies of LALSuite and PyCBC, that should be used instead of the original environment file in LALSuite to create a virtual environment for the installation. Also the `requirements.txt` and `companion.txt` files from PyCBC are replaced by this. To ensure the locally build version of LALSuite is used its appearance in the `setup.py` file as a PyCBC dependency was removed.

5. Computation

5.1. Cluster usage

To provide the needed computation power the inferences were run on two clusters: either the cluster of the Institute for Theoretical Physics [42] or to be more correct on its *itp* partition and the FUCHS cluster of the Center for Scientific Computing Frankfurt [43]. Both are linux based with Xeon Ivy Bridge 10 core, 20 thread processors on their compute nodes, but the FUCHS cluster nodes are dual socket machines resulting in twice the number of threads per node.

They both use *slurm* [44] an open source workload manager as a user interface to run jobs. This also supports MSI, which allows *pycbc_inference* to split its tasks in an optimal way and also between different nodes. The way *slurm* works is by queuing jobs until the desired resources can be dedicated. Then the job, in our case a bash script, is copied and executed in a temporary directory (Dir) on the compute nodes. But *slurm* still has to interface with the original file system (FS), which typically is the place of the *user* Dir, for installed libraries, configuration files or to save the output. This is much slower than the *local* tree of the compute nodes. To counteract this both cluster have a data storage with much higher bandwidth designated for large data sets. For the FUCHS cluster figure 7 shows the setup of the data storage and for the ITP cluster a good description can be found in [45].

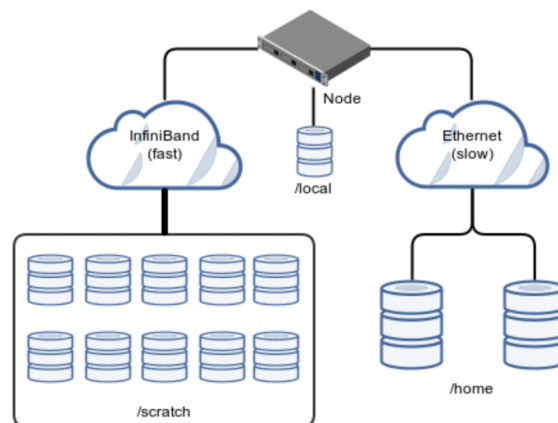


Figure 7: Data storage design of the FUCHS cluster (reprinted from [43], Storage).

By that the preferred setup also used here is using the *ceph* or *scratch* FS during the jobs and using the *user* Dir only sparsely for important files, installation of packages, libraries etc. Because the space on this is fairly limited and missing space at any time will result in a stop of the inference and by that the end of the *slurm* job, the workflow should be also robust to that allowing for a continuation with reduced functionality, when only the much larger *scratch* FS is available.

5.2. Submission scripts

Although the *sbatch* command of slurm allows for very simple job definitions in preprocessor commands, because of the mentioned complex setup I have written a script to provide an interface to *sbatch*. The goal is that a user can submit a job without making any changes to the script and it works as if it was executed in its original directory without even using slurm. For the synchronisation between FSs the very robust, but also efficient tool *rsync* is used. [46]

The first part *sbatchIt.sh* fully shown in the attached listing [7] provides all options needed for this. Its setup with optional inputs as flags (lines 10 – 41) deals very well with the combination of settings which most of the time will be the same and settings a user wants to adapt usually. By that it has the same syntax as the original *sbatch* command and also contains a *help* section, which states all possible options. The only compulsory input is the script, which should be run in the slurm job. All this can be seen in listing [8] for the user input handling. In addition to this, the script can handle relative paths and is robust to all places of execution to be more user friendly.

```

5  ### simlinked directory and cluster partion -- edit before first use \\  

   !!! ###  

6  

7  lnkDir="$HOME/runD/linked"  

8  part="fuchs"  

9  

10 ### process user input ###  

11  

12 # define std values  

13 orgDir=$(readlink -f $lnkDir)  

14 exeIn="$orgDir/script1/" # scrip1 in symlinked directory  

15 clear=0                 # no clearing  

16 tasks=20                # MSI taskcount of 20  

17 timeLim=21-0:00  

30  

31 # flags in user input:  

32 # c for clearing of surrounding befoe sync, d for nonstd directory, \<\  

   n for nodecount, t for time limit  

33 while getopts ce:hn:t: opt; do  

34     case $opt in  

35         c) clear=1;;  

36         e) exeIn="$orgDir/$OPTARG";;  

37         h) printf "$hlp"; exit;;  

38         n) tasks=$OPTARG;;  

39         t) timeLim=$OPTARG;;  

40     esac  

41 done  

42  

43 # needed input: script to be run  

44 script=${@:$OPTIND:1}

```

Listing 3: Lines in *sbatchIt.sh* to handle the user input, so the syntax is equivalent to *sbatch*.

To make the interfacing with the *scratch* FS simpler, the only task for the user is to create a symbolic link (symlink) to his *scratch* Dir, which has to be placed in the same Dir as *sbatchIt.sh*. Before the first use its path has to be put into the file at line 7 as well as the partition name of the used cluster.

After all input and path processing is done it informs the user how the execution will happen from line 61 onwards (listing 4) and asks, if a job should be queued under these conditions. As a part of this the *test-only* feature of the *sbatch* command is used in line 75 to give a hint on the estimated starting time.

```
61 # inform user, what will be done
62 echo "execute_$name_from_$dir"
63 echo "in_$exeIn"
64 if [ $clear -gt 0 ]; then
65     echo "which_will_be_cleared_first"
66 fi
67 echo "using_srun.sh_in:"
68 pwd
69 echo "test_of_queuing:"
70
71 #ensure existence of log directory
72 mkdir -p $orgDir/log
73
74 # sbatch test run
75 sbatch -p $part -t $timeLim -n $tasks -o "$orgDir/log/slurm-%j.out" \\  
    -e "$orgDir/log/slurm-%j.out" --test-only srun.sh $dir $name \\  
    $exeIn $clear
76
77 # ask user if he wants to queue job or exit
78 while true; do
79     read -p "Do_you_want_to_queue_at_this_conditions?(y/n)" yn
80     case $yn in
81         [yY] ) break;;
82         [nN] ) exit;;
83         * ) echo invalid response;;
84     esac
85 done
86
87 #queue job
88 sbatch -p $part -t $timeLim -n $tasks -o "$orgDir/log/slurm-%j.out" \\  
    -e "$orgDir/log/slurm-%j.out" srun.sh $dir $name $exeIn $clear
89 echo "queuing_done"
```

Listing 4: Last part of *sbatchIt.sh* for interactive queueing with a test run before asking the user for acceptance to do so.

Because functions and virtual shell wrapping are not very well supported by *sbatch*, everything which should be done inside the job is placed in a second script *srun.sh* (the complete file can be found in listing 8). This should be placed in the same Dir as well and is executed by *sbatchIt.sh*.

It takes four preprocessed inputs: The name and the original Dir from the script the user wants to execute as well as where inside the linked Dir it should be executed and if this should be cleared first. The idea for this is to allow for parallel jobs and also sequential use of the same execution Dir without starting from zero. With these the *cpSur* function (lines 7 – 26 in listing 5) copies everything besides old slurm results into the specified Dir.

```

7 cpSur() {
8     # define origin and destination inputs
9     orgn=$1
10    dest=$2
11    B00Lclr=$3
12
13    # create destination dir if not existing
14    mkdir -p $dest
15
16    # clean before sync, if flag set
17    if [ $B00Lclr -gt 0 ]; then
18        rm -r $dest/*
19        echo "cleaned"
20    fi
21
22    # sync files without former slurm results
23    rsync -achE --delete --exclude 'slurm*' $orgn/* $dest/
24
25    echo "sync_to_${dest}_done"
26 }

```

Listing 5: Definition of the *cpSur* function creating an equivalent local tree to the scripts original surrounding in the new symlinked directory, so for example relative paths still work.

After that a timestamp is saved and the user's script is executed in lines 69 and following. When this has finished the *saveRes* function (lines 29 – 53, shown in listing 6) handles the synchronisation back to the original Dir. For this in an intermediate step a new Dir is created in the symlinked Dir with the slurm job id were all files changed or created after the set timestamp are copied into. Also the *sbatch* output and error files are moved into this. At last the synchronisation back to the origin is tried for this Dir. If it fails only a text file with a short message and the path to the data is created there. By that in the case of missing space to save the results in the user Dir the job can still finish successfully. The only difference is, that to get to the results the user has to go to the path in the written file, instead of finding them in a created directory with the same name.

```
29 saveRes() {
30     # define inputs for start time and directory to sync to
31     startT=$1
32     resDir=$2
33
34     # create directory with name of slurm job
35     jobname="slurm${SLURM_JOB_ID}"
36     mkdir ../$jobname
37     jobdir=$(cd ../; readlink -f $jobname)
38
39     # sync result files to created directory
40     echo "results_in_files:"
41     find . -type f -newermt $startT
42     find . -type f -newermt $startT -print0 | rsync -ach \\  
        --include-from=- $jobdir
43
44     echo "sync_to_${jobdir}_done"
45
46     # mv slurm log file to this
47     cp ../log/*${SLURM_JOB_ID}.* $jobdir/.
48
49     # try to sync results to origin directory of the script, create \\  
        error file otherwise
50     mkdir $resDir/$jobname
51     rsync -achE $jobdir/* $resDir/$jobname/ || (rm -r \\  
        $resDir/$jobname; echo "sync_failed,_data_in_{$jobdir}" >> \\  
        $resDir/$jobname)
52     echo "sync_to_{$resDir}/{$jobname}_done"
53 }
```

Listing 6: Definition of the *saveRes* function collecting modified files and *slurm* output and copying them back in the original directory.

6. Conducted inferences

6.1. The GW170817 Event

The carried out inferences were done for the gravitational wave event detected by LIGO and Virgo in August 2017. For this the original analysis can be found in [47]. It was the first and until now only certain NS-NS merger event of the LIGO observations, for which also an optical counterpart in form of a gamma ray burst (GRB) was detected by the Fermi telescope called GRB170817A. [48]

The observed strain can be found in figure 8, which shows the chirping nature of the signal until the merger at $\tau = 0$ very nicely. Because of its far better signal-to-noise-ratio (SNR) only the data from the LIGO observatory are used in this work.

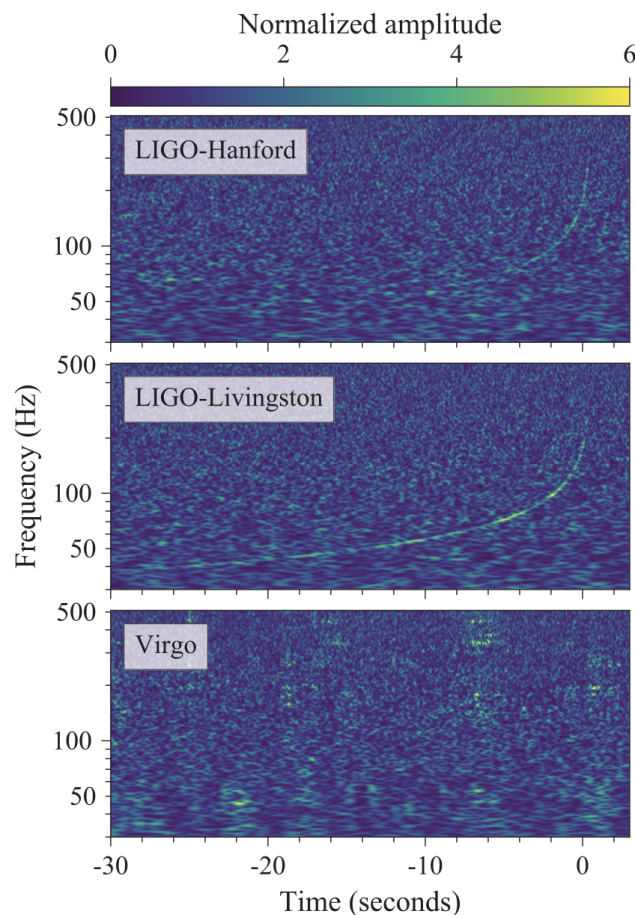


Figure 8: Data from the GW170817 event observed by LIGO-Hanford, LIGO-Livingston and Virgo in a time-frequency-representation showing the chirp signal very nicely for both LIGO detectors (reprinted from [47, fig. 1]).

The results of the original analysis, which was an inference based on the signal in the range of 20 Hz to 2048 Hz, can be found in table 2 together with the information one can get from the optical counterpart. These will be the reference for the following analyses done by myself. Like in the analysis by LIGO for the TD it was assumed that $k_2 \approx 0.10(5)$ for NSs, which can be found in [47, ch. IV].

LIGO analysis	Low-spin priors	High-spin priors
Primary mass m_1	1.36–1.60 M_\odot	1.36–2.26 M_\odot
Secondary mass m_2	1.17–1.36 M_\odot	0.86–1.36 M_\odot
Chirp mass M_c	1.188 $^{+0.004}_{-0.002}M_\odot$	1.188 $^{+0.004}_{-0.002}M_\odot$
Mass ratio m_2/m_1	0.7–1.0	0.4–1.0
Total mass M	2.74 $^{+0.04}_{-0.01}M_\odot$	2.82 $^{+0.47}_{-0.09}M_\odot$
Luminosity distance D_L	40 $^{+8}_{-14}$ Mpc	40 $^{+8}_{-14}$ Mpc
Viewing angle θ	$\leq 55^\circ$	$\leq 56^\circ$
Comb. tidal deformability $\tilde{\Lambda}$	≤ 800	≤ 700
GRB positional properties		
Luminosity distance D_L	40.7 Mpc	
Right ascension ra	(176.8 \pm 11.6) $^\circ$	
Declination dec	(-39.8 \pm 11.6) $^\circ$	

Table 2: Reconstructed parameters of the GW170817 system resulting from the original LIGO analysis [47, tab. 1] and GRB counterpart [48, tab. 1].

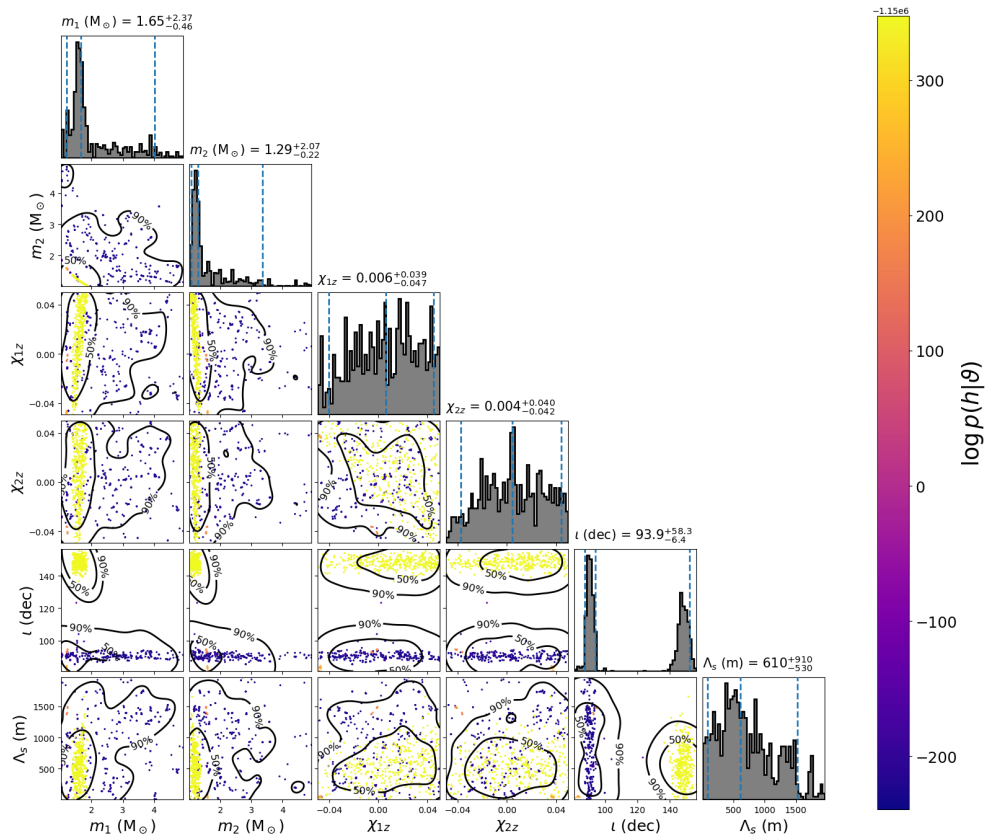
6.2. Sampler evaluation

Like stated in 4.3 together with the prior choice and the waveform model the selection of the sampler is one of the most important parts ensuring the correctness of the inference results. To test for the difference of the two well-supported samplers *eemce* and *eemce_pt* regarding exploration of the parameter space and efficiency otherwise identical runs were started for both of them.

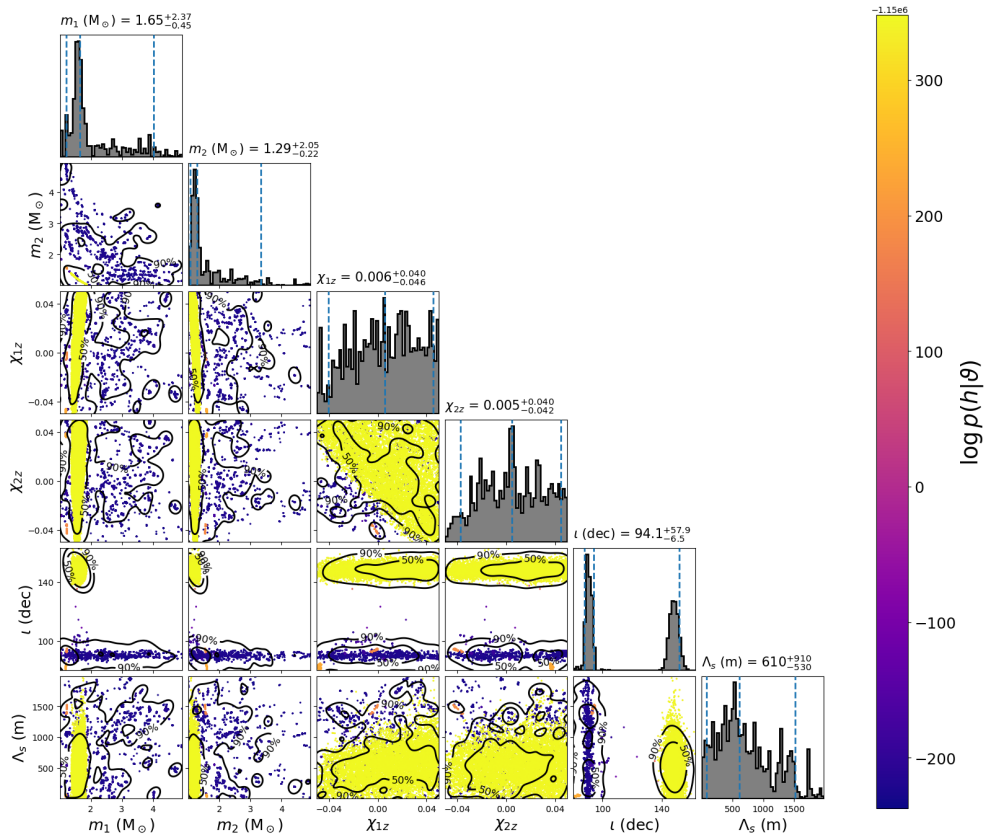
Listing 10 containing the file *GW170817GR.ini* shows the included parameters and its priors: Like in the LIGO analysis a lower cutoff of 20 Hz was used, the priors were all chosen to be uniform (lines 55-128), the position in space from the GRB was set as static parameters (lines 38-41) and the *TaylorF2*-waveform was used. This includes the modified version of the tidal deformability described in 4.4, but by setting the axion parameters to 0 one resembles the GR-case (lines 50-53). For the data the files from the Gravitational Wave Open Science Center [49] with subtracted noise were used. The configuration of their injection for the likelihood function defined in *data.ini* is shown in listing 12, in which a resampling to 2048 Hz was put in place. Additionally listing 9 shows an example of the script for calling *pycbc_inference*.

For the *eemce* sampler a run with 100 walkers was conducted (listing 13). For this as well as *eemce_pt* the masses were transformed into chirp mass and mass ratio before sampling and the included burn-in tests were used. The *max_posterior* test was never true. The reason for this can be the high number of variables effectively shrinking the surrounding area. But the *nacl* test, was true even for the first checkpoint. By that the burn-in phase is the first half of the chains. This test, the ACL to be precise, is also the foundation for the calculated effective samples. This part is not working as intended, so the plots with thinned chains all only contain around 800 samples independent of their overall number.

Figure 9a shows the results for only the automatically chosen effective samples and figure 9b shows the plot with all samples after the burn-in phase for comparison. Comparing the parameter values to table 2 the masses fit quite well, although the secondary mass is a bit smaller than in the original analysis. Also for the symmetric TD the value is similar, but the confidence interval is a lot broader, which can also be seen from the shape of its histogram. The comparison of the spins is not that easy, because only the z-component was taken into account, but the distributions show that the low spin assumption as a possible case is valid. The inclination shows two possible viewing angles. It could be almost 0° or around 55° . This also is not conflicting the LIGO constrain of being below 55° .



(a) Chains thinned by using only the effective samples from *nacl*.



(b) Complete second halves of the chains after burn-in.

Figure 9: The marginalised posteriors for the GR case using the *emcee* sampler and showing the masses and spins in z-direction of the two NSs as well as the inclination ι and symmetric TD Λ_s (The coalescence time and phase are not shown, because they were only included to optimise the analysis and have very thin peaks around their actual value).

Despite the fact that the resulting values seem reasonable the results should be taken with a grain of salt. The shape of all distributions show at least large fluctuations around the form of a Gaussian. This could be only an artefact of the small sample size and missing thinning respectively. But it can still have a significant impact on the values and especially the confidence intervals of the parameters.

For *eemce_pt* the sampling was set up with 10 different temperatures for the 100 chains shown in listing [14](#). The results of this run are shown in figure [10](#). With the computation time per iteration being almost 5 times large than using *eemce* it was definitely more computational expensive. Also a doubling of the threads to 160 resulted only in a 20 % decrease, which proofs as not very efficient and cannot compensate for the additional complexity. Because of that the run was interrupted after 4000 iterations, which took almost the same computation time as the *eemce* run. In spite of that the usage of this sampler can be useful because the ACL was for each checkpoint roughly 10 times smaller, leading to more effective samples.

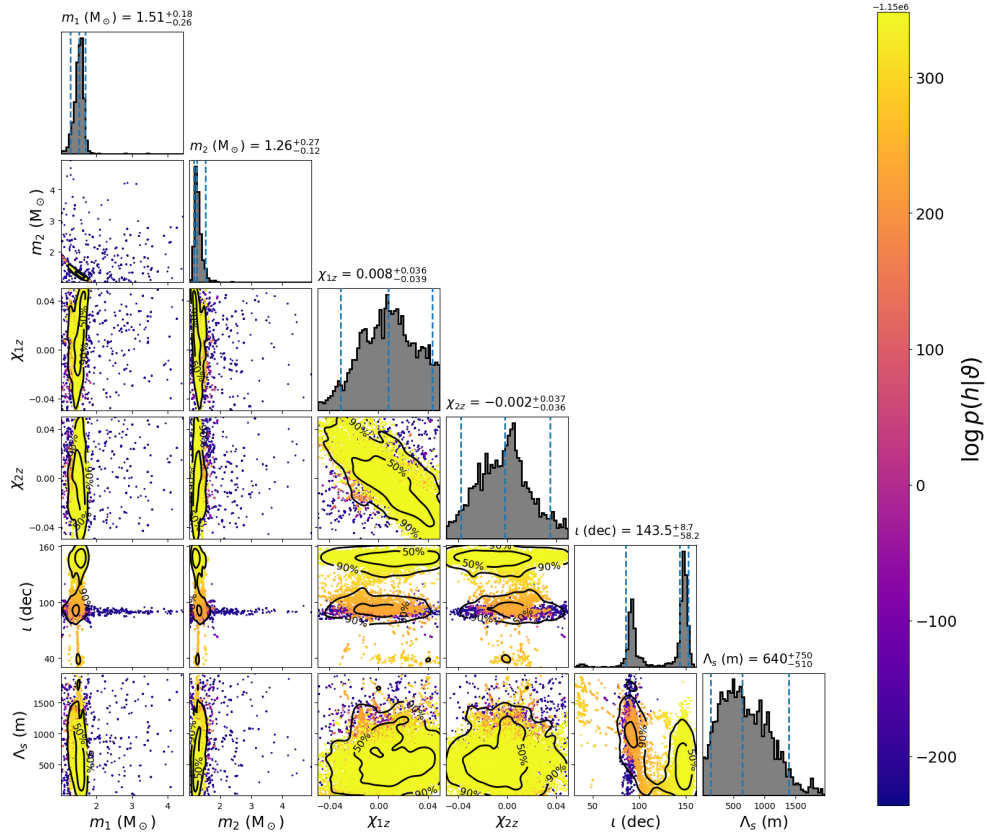


Figure 10: The marginalised posteriors for the GR case using the *emcee_pt* sampler and showing the masses and spins in z-direction of the two NSs as well as the inclination i and symmetric TD Λ_s .

The difference in the values of the parameters in comparison to figure 9 are small but exist: The masses are even a bit smaller, the z-component of ξ_1 is of the same order of magnitude and for the TD the confidence interval starts to resemble the constrain from the original analysis. Interesting are also the distributions: In the scatter plots the number of points far from the maxima seem to be fewer and the shapes of the marginalised posteriors are smoother. The most significant change is in the posterior of i . Here the second peak at 54° is now dominant. By this the superior exploration of the *emcee_pt* sampler really seems to make a difference, but to give a final verdict on this also in this case it would be necessary to have the posteriors after a well working thinning process.

6.3. Axion search

Even though there still are some difficulties for the sampler. An inference with the additional parameters for the axion charge shown in [3.1](#) were conducted with the *emcee* sampler. The definition of new variables can be found in listing [11](#), lines 26-29 as well as the definition of their uniform priors. In addition to this the Compton wavelength λ_a was fixed to 2×10^5 m. The sampling parameters and data were the same as for the GR case resulting in the priors shown in figure [11](#).

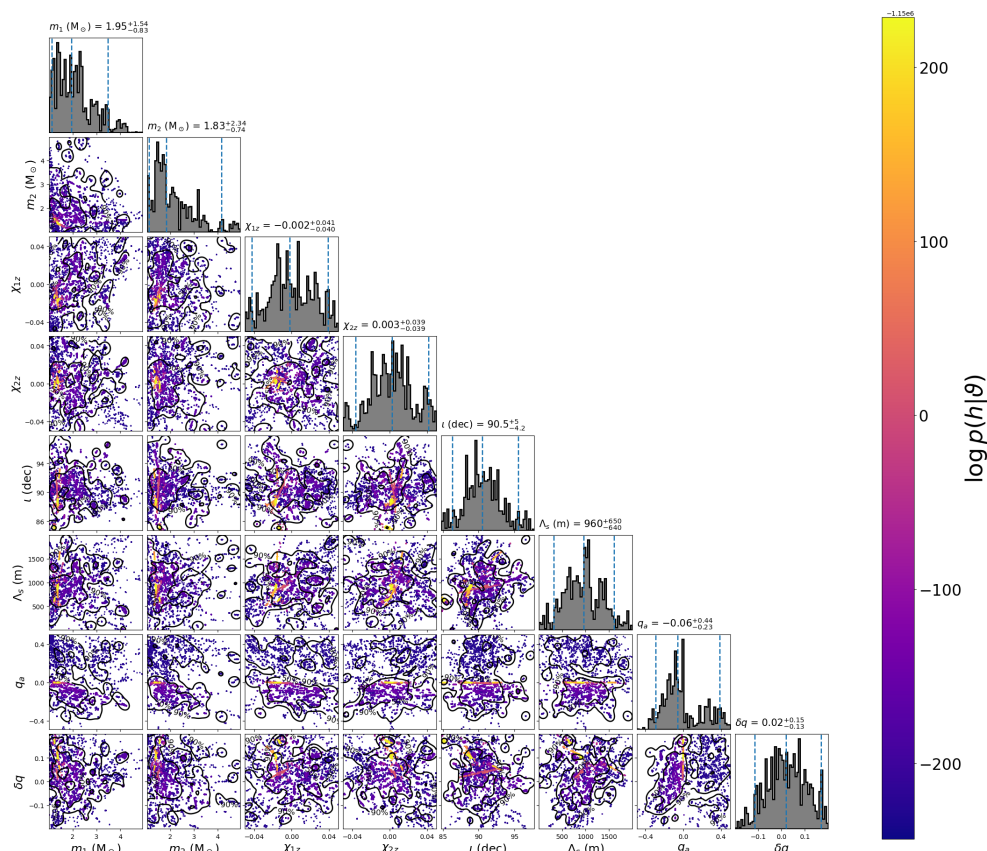


Figure 11: Results for the axion case using the *emcee* sampler and showing all samples after the burn-in phase.

Here the main difference for the parameters also present in the GR case is, that the masses are much higher, but with under $2 M_\odot$ still reasonable. In the posterior of the inclination the two peaks cannot be distinguished anymore, because the shape of the posteriors has degraded, which may be due to the higher dimensionality. By that also for the axion parameters charge q and charge difference between the NSs δq there is a non-optimal picture. These have mean values around 0, which would resemble the GR case, but the distributions are very broad and have high fluctuations. So based on this analysis it is hard to make a statement about the presence of axions.

7. Conclusion & outlook

Binary NS are good systems for analysing the waveform for information not only about the system itself, but also about the nature of the attracting force and by that its difference to the predictions of GR. With the approach of Bayesian inferences being a good way to get reliable information about the quantities influencing the waveform, PyCBC is in principle a useful tool for this analysis. But its complexity also leads to difficulties, especially if the code has to be modified like in our case. Also that NS events are much less common, are in a different mass range and result in another type of wave form creates challenges, because good documentation, example cases etc. are not as common for this case. The difficulties for using the sampler and the in-built burn-in tests also showed that further investigations in these are necessary to achieve a reliable method also for analysing the discussed event, which is a different to the others.

In addition to that for probing ALPs having only one system with one realisation of the possible masses makes it difficult to test the large parameter space for the masses and decay rates. But even the analysis for $\lambda_a = 200\,000\text{ m}$ only showed that it is possible that this value has to be exclude for possible ALPs, but it could not show strong enough evidence to do so. More detections especially with larger masses could help to make the evidence clearer. So further analyses as soon as the data from the observation run O4 will become available should be done. For these it will be essential to optimise the efficiency of the sampling for this type of systems, before conducting all the inferences for the different events, which hopefully will be detected.

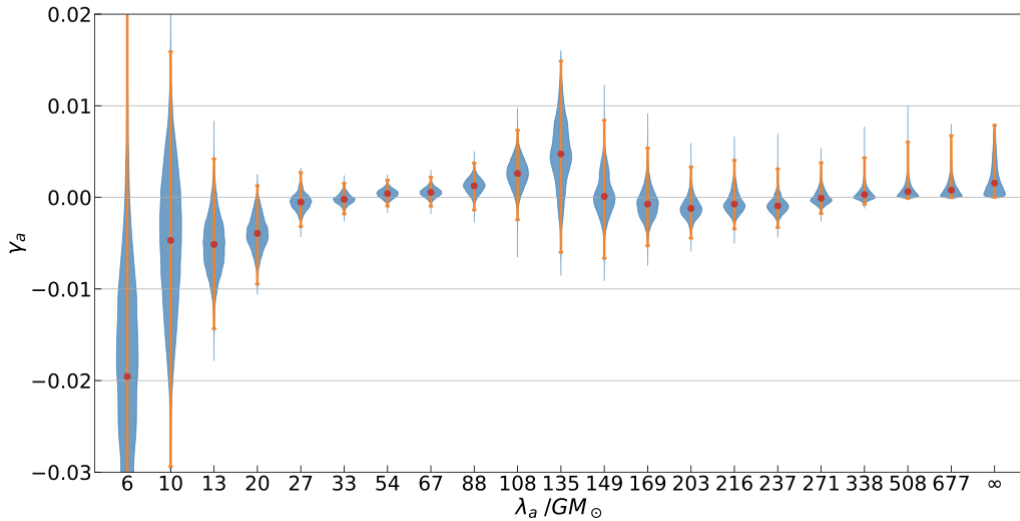


Figure 12: Posteriors for axions with different masses $1/\lambda_a$ for a parameter for the combined charges $\gamma_a \propto q_1 q_2$ showing small standard deviations for small enough masses besides at a degeneracy with the chirp mass around $135\text{ }GM_\odot$ (reprinted from [19, fig. 2]).

After the optimisation of the inferences the final goal of the project regarding axions will be to produce constrains for the axion parameters mass and decay rate. By doing the analysis for several λ_a like shown in figure 12 one can see, if there is evidence for certain types of these or if this part of the parameter space has to be excluded. It also shows in which mass range the effect is significant and this distinction can even be made. Finally a constrain plot analog to what was done in 19 and is shown in figure 13 should be produced. In the corresponding paper there was a mistake regarding the implementation of the TD in the modified *TaylorF2* waveform described in section 4.4. So a further analysis should show, if this made a difference in the final constrains, resulting in the need for a correction of these .

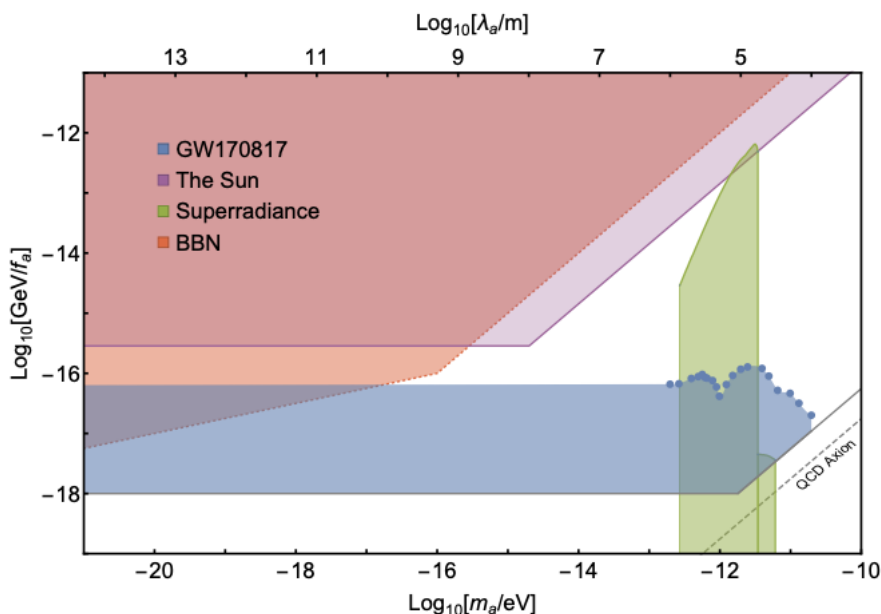


Figure 13: Constrains on the masses and decay rate of axion fields from GW170817 corresponding to 3σ (blue). Additionally constrains from big bang nucleosynthesis (green) and the spin of stellar mass black holes (red) are depicted (reprinted from 19, fig. 1).

A next step will also be to evaluate the results for $f(R)$ -gravity by matching the two parameters to a_2 and produce a similar constrain plot. Additionally, the versatility of the scalar field model would make possible to look for different modifications of GR and maybe even effects of quantum gravity 50, ch. 32] encoded in the waveform.

A. Code structure

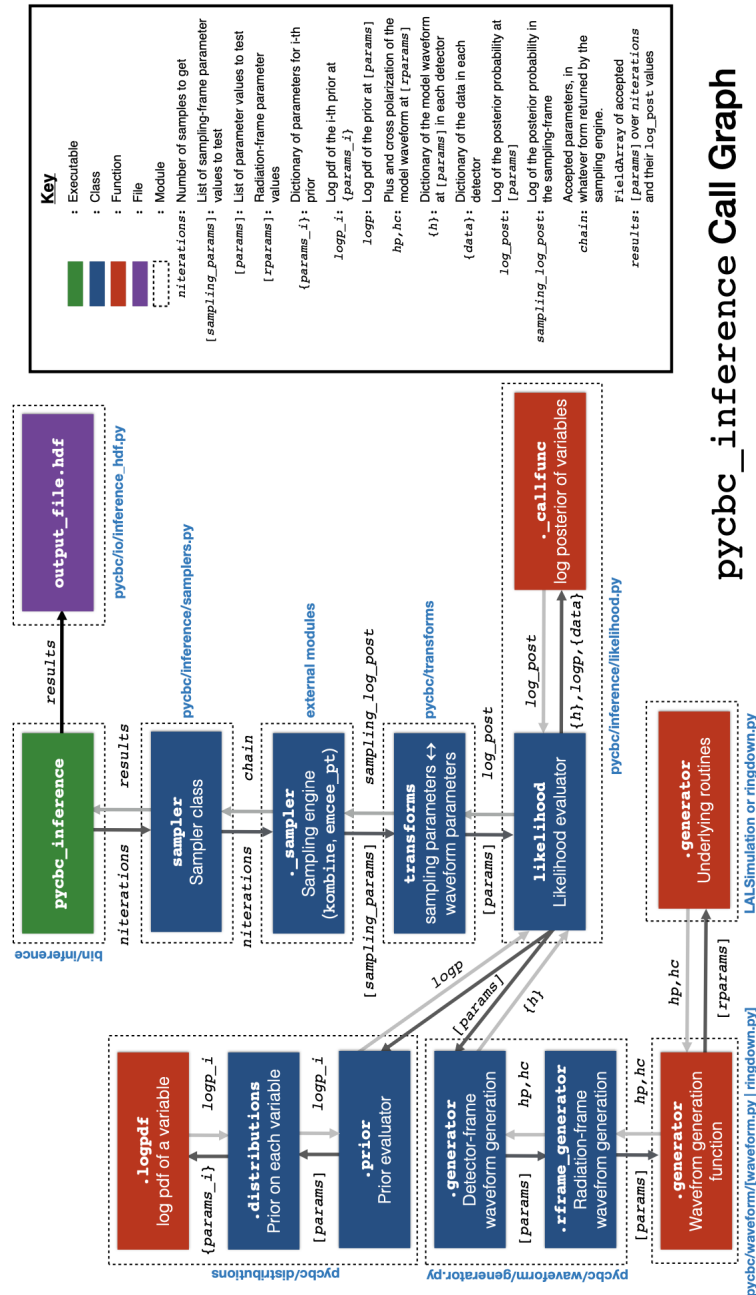


Figure 14: The call graph for the `pycbc_inference` executable showing the data flow from the input modules and the waveform generation on the left to the sampling process in the middle row to the outputted data file and posteriors on the right. (reprinted from [35], fig. 2).

B. Submission scripts

```

1 #!/bin/bash
2 # run bash script via slurm in ceph fs (simlinked folder in same \
   directory needed)
3 # supported flags: c for clearing of surrounding before sync, d for \
   nonstd directory, n for corecount, t for timelimit
4
5 ### simlinked directory and cluster partion -- edit before first use \
   !!! ###
6
7 lnkDir="$HOME/runD/linked"
8 part="fuchs"
9
10 ### process user input ###
11
12 # define std values
13 orgDir=$(readlink -f $lnkDir)
14 exeIn="$orgDir/script1/" # scrip1 in symlinked directory
15 clear=0                 # no clearing
16 tasks=20                # MSI taskcount of 20
17 timeLim=21-0:00
18
19 # text for help flag:
20 hlp="Script_for_usage_of_sbatch_on_cluster_partition_${part},\n"
21 hlp+="while_executing_in_scratch_fs_directory_${orgDir}.\n"
22 hlp+="\n"
23 hlp+="Usage:_bash_sbatchIt.sh_[OPTIONS...]\_executable_[args...]\n"
24 hlp+="With_possible_options:\n"
25 hlp+="-c_clear_scratch_directory_before_syncing_it\n"
26 hlp+="-d_execute_in_directory_other_than_script1_(given_by_argument)\n"
27 hlp+="-h_help\n"
28 hlp+="-n_number_of_threads_to_be_allocated_for_MSI_tasks\n"
29 hlp+="-t_time_limit_in_days-hours\n"
30
31 # flags in user input:
32 # c for clearing of surrounding befoe sync, d for nonstd directory, \
   n for nodecount, t for time limit
33 while getopts ce:hn:t: opt; do
34     case $opt in
35         c) clear=1;;
36         e) exeIn="$orgDir/$OPTARG";;
37         h) printf "$hlp"; exit;;
38         n) cores=$OPTARG;;
39         t) timeLim=$OPTARG;;
40     esac
41 done
42
43 # needed input: script to be run
44 script=${@:$OPTIND:1}
45

```

```

46 # switch error handling on, to quit on error in single command
47 set -e
48
49 # get filename and directory from absolute path
50 path=$(readlink -f $script)
51 dir="$(dirname "${path}")"
52 name="$(basename "${path}")"
53
54 # change to directory this script is placed in
55 itself=$(readlink -f $0)
56 here="$(dirname "${itself}")"
57 cd $here
58
59 ### slurm part ###
60
61 # inform user, what will be done
62 echo "execute_${name}_from_${dir}"
63 echo "in_${exeIn}"
64 if [ $clear -gt 0 ]; then
65     echo "which_will_be_cleared_first"
66 fi
67 echo "using_srun.sh_in:"
68 pwd
69 echo "test_of_queuing:"
70
71 #ensure existence of log directory
72 mkdir -p $orgDir/log
73
74 # sbatch test run
75 sbatch -p $part -t $timeLim -n $tasks -o "$orgDir/log/slurm-%j.out" \\\
    -e "$orgDir/log/slurm-%j.out" --test-only srun.sh $dir $name \\\
    $exeIn $clear
76
77 # ask user if he wants to queue job or exit
78 while true; do
79     read -p "Do_you_want_to_queue_at_this_conditions?(y/n)" yn
80     case $yn in
81         [yY] ) break;;
82         [nN] ) exit;;
83         * ) echo invalid response;;
84     esac
85 done
86
87 #queue job
88 sbatch -p $part -t $timeLim -n $tasks -o "$orgDir/log/slurm-%j.out" \\\
    -e "$orgDir/log/slurm-%j.out" srun.sh $dir $name $exeIn $clear
89 echo "queuing_done"

```

Listing 7: *sbatchIt.sh*, script that queues *slurm* job and handles user input of *sbatch* options and paths.

```
1 #!/bin/bash
2 # script to be called by sbatch in sbatchIt.sh
3
4 ### definition of functions ###
5
6 # copy surrounding files to scratch directory
7 cpSur() {
8     # define origin and destination inputs
9     orgn=$1
10    dest=$2
11    B00Lclr=$3
12
13    # create destination dir if not existing
14    mkdir -p $dest
15
16    # clean before sync, if flag set
17    if [ $B00Lclr -gt 0 ]; then
18        rm -r $dest/*
19        echo "cleaned"
20    fi
21
22    # sync files without former slurm results
23    rsync -achE --delete --exclude 'slurm*' $orgn/* $dest/
24
25    echo "sync_to_${dest}_done"
26 }
27
28 # function to sync results to lasting directories
29 saveRes() {
30     # define inputs for start time and directory to sync to
31     startT=$1
32     resDir=$2
33
34     # create directory with name of slurm job
35     jobname="slurm${SLURM_JOB_ID}"
36     mkdir ../$jobname
37     jobdir=$(cd ../; readlink -f $jobname)
38
39     # sync result files to created directory
40     echo "results_in_files:"
41     find . -type f -newermt $startT
42     find . -type f -newermt $startT -print0 | rsync -ach \
43         --include-from=- $jobdir
44
45     echo "sync_to_${jobdir}_done"
46
47     # mv slurm log file to this
48     cp ../log/*${SLURM_JOB_ID}.* $jobdir/.
```

```

49 # try to sync results to origin directory of the script, create \\  

    error file otherwise  

50 mkdir $resDir/$jobname  

51 rsync -achE $jobdir/* $resDir/$jobname/ || (rm -r \  

    $resDir/$jobname; echo "sync_failed,_data_in_{$jobdir}" >> \  

    $resDir/$jobname)  

52 echo "sync_to_{$resDir}/{$jobname}_done"  

53 }  

54  

55 # function for everything which should be put into slurm job  

56 tbQueued() {  

57 # define all input variables  

58 orgn=$1 # path to original directory  

59 script=$2 # name of script to be run  

60 exeIn=$3 # directory script to be run in  

61 B00Lclr=$4 # bool to decide, if to clear before syncing  

62 echo "execute_{$script}_from_{$orgn}"  

63 echo "in_{$exeIn}"  

64  

65 # sync directory of execution with origin  

66 cpSur $orgn $exeIn $B00Lclr  

67 cd $exeIn  

68  

69 # set timestamp before execution of script  

70 startT="@$(date +%s)"  

71 echo "start_time_{$startT}"  

72  

73 # run script in ceph directory  

74 echo "execute_{$script}:"  

75 /bin/bash $script  

76  

77 # save results back in original directory  

78 cd $exeIn  

79 saveRes $startT $orgn  

80 }  

81  

82 ### final function call ###  

83 tbQueued $1 $2 $3 $4

```

Listing 8: *srn.sh*, syncing to *ceph* FS and executing handed script inside the *slurm* job.

C. Inference files

```
1 #!/bin/bash
2 # pycbc inference script
3
4 # configuration files
5 PRIOR_CONFIG=GW170817GR.ini
6 DATA_CONFIG=data.ini
7 SAMPLER_CONFIG=emcee.ini
8
9 # output data file
10 OUTPUT_PATH=inference.hdf
11
12 # the following sets the number of cores to use; adjust as needed to
13 # your computer's capabilities
14 NPROCS=80
15 PROCESSING_SCHEME=cpu
16
17 # change directory for using relative paths
18 itself=$(readlink -f $0)
19 here="$(dirname "${itself}")"
20 cd $here
21
22 # run sampler
23 # Running with OMP_NUM_THREADS=1 stops lalsimulation
24 # from spawning multiple jobs that would otherwise be used
25 # by pycbc_inference and cause a reduced runtime.
26 OMP_NUM_THREADS=1 \
27 pycbc_inference --verbose \
28   --seed 1897234 \
29   --config-file $PRIOR_CONFIG $DATA_CONFIG $SAMPLER_CONFIG \
30   --output-file $OUTPUT_PATH \
31   --nprocesses $NPROCS \
32   --processing-scheme $PROCESSING_SCHEME \
33   --use-mpi \ # necessary for dividing in single thread slurm tasks
34   --force
```

Listing 9: *run.sh*, script for calling *pycbc_inference* for the GR case.


```
1 ; GR case priors with q=dq=0 and GRB info
2
3 ; assume Gaussian noise in signal
4 [model]
5 name = gaussian_noise
6 low-frequency-cutoff = 20.0
7
8 ; waveform parameters that will vary in MCMC
9 [variable_params]
10 delta_tc =
11
12 mass1 =
13 mass2 =
14
15 spin1z =
16 spin2z =
17
18 ;ra =
19 ;dec =
20 ;distance =
21
22 coa_phase =
23 inclination =
24 polarization =
25
26 ; axion specific parameters
27 ;tidal_ls =
28 ;axion_q =
29 ;axion_dq =
30
31 ; waveform parameters that will not change in MCMC
32 [static_params]
33 ; TaylorF2 waveform template
34 approximant = TaylorF2
35 f_lower = 15
36 f_ref = 0
37
38 ; from GRB counterpart
39 ra = 3.44615914
40 dec = -0.40808407
41 distance = 40.7
42
43 ; trigger time from data file
44 trigger_time = ${data|trigger-time}
45
46 ; axionlambda in unit of meters
47 ; (lambda < 0 -> massless)
48 axion_lambda = 200000
49
```

```
50 ; turn axion effects of
51 axion_q = 0
52 axion_dq = 0
53 axion_p = 0
54
55 ; coalescence time prior
56 [prior-delta_tc]
57 name = uniform
58 min-delta_tc = -0.1
59 max-delta_tc = 0.1
60
61 ; we'll set the tc by using the trigger time in the data
62 ; section of the config file + delta_tc
63 [waveform_transforms-tc]
64 name = custom
65 inputs = delta_tc
66 tc = ${data|trigger-time} + delta_tc
67
68 ; mass priors
69 [prior-mass1]
70 name = uniform
71 min-mass1 = 1.
72 max-mass1 = 5.
73
74 [prior-mass2]
75 name = uniform
76 min-mass2 = 1.
77 max-mass2 = 5.
78
79 ; priors for spins in z-direction
80 ; (only coordinate used in TaylorF2)
81 [prior-spin1z]
82 name = uniform
83 min-spin1z = -0.05
84 max-spin1z = 0.05
85
86 [prior-spin2z]
87 name = uniform
88 min-spin2z = -0.05
89 max-spin2z = 0.05
90
91 ;[prior-distance]
92 ;name = uniform_radius
93 ;min-distance = 20
94 ;max-distance = 100 name = uniform
95
96 ;[prior-ra+dec]
97 ; sky position prior
98 ;name = uniform_sky
99
```

```
100 ; coalescence phase prior
101 [prior-coa_phase]
102 name = uniform_angle
103
104 ; inclination prior
105 [prior-inclination]
106 name = sin_angle
107
108 ; polarization prior
109 [prior-polarization]
110 name = uniform_angle
111
112 ; sym. tidal deformability prior
113 [prior-tidal_ls]
114 name = uniform
115 min-tidal_ls = 0
116 max-tidal_ls = 2000
117
118 ; axion charge prior
119 [prior-axion_q]
120 name = uniform
121 min-axion_q = -0.5
122 max-axion_q = 0.5
123
124 ; axion charge difference prior
125 [prior-axion_dq]
126 name = uniform
127 min-axion_dq = -0.2
128 max-axion_dq = 0.2
```

Listing 10: *GW170817GR.ini*, configuration file for GR-case inference parameters and priors.

```
1 ; Axion case priors with GRB info
2
3 ; assume Gaussian noise in signal
4 [model]
5 name = gaussian_noise
6 low-frequency-cutoff = 20.0
7
8 ; waveform parameters that will vary in MCMC
9 [variable_params]
10 delta_tc =
11
12 mass1 =
13 mass2 =
14
15 spin1z =
16 spin2z =
17
18 ;ra =
19 ;dec =
20 ;distance =
21
22 coa_phase =
23 inclination =
24 polarization =
25
26 ; axion specific parameters
27 tidal_ls =
28 axion_q =
29 axion_dq =
30
31 ; waveform parameters that will not change in MCMC
32 [static_params]
33 ; TaylorF2 waveform template
34 approximant = TaylorF2
35 f_lower = 15
36 f_ref = 0
37
38 ; from GRB counterpart
39 ra = 3.44615914
40 dec = -0.40808407
41 distance = 40.7
42
43 ; trigger time from data file
44 trigger_time = ${data|trigger-time}
45
46 ; axionlambda in unit of meters
47 ; (lambda < 0 -> massless)
48 axion_lambda = 200000
49
```

```
50 ; look for axions
51 ;axion_q = 0
52 ;axion_dq = 0
53 axion_p = 0
54
55 ; coalescence time prior
56 [prior-delta_tc]
57 name = uniform
58 min-delta_tc = -0.1
59 max-delta_tc = 0.1
60
61 ; we'll set the tc by using the trigger time in the data
62 ; section of the config file + delta_tc
63 [waveform_transforms-tc]
64 name = custom
65 inputs = delta_tc
66 tc = ${data|trigger-time} + delta_tc
67
68 ; mass priors
69 [prior-mass1]
70 name = uniform
71 min-mass1 = 1.
72 max-mass1 = 5.
73
74 [prior-mass2]
75 name = uniform
76 min-mass2 = 1.
77 max-mass2 = 5.
78
79 ; priors for spins in z-direction
80 ; (only coordinate used in TaylorF2)
81 [prior-spin1z]
82 name = uniform
83 min-spin1z = -0.05
84 max-spin1z = 0.05
85
86 [prior-spin2z]
87 name = uniform
88 min-spin2z = -0.05
89 max-spin2z = 0.05
90
91 ;[prior-distance]
92 ;name = uniform_radius
93 ;min-distance = 20
94 ;max-distance = 100 name = uniform
95
96 ;[prior-ra+dec]
97 ; sky position prior
98 ;name = uniform_sky
99
```

```
100 ; coalescence phase prior
101 [prior-coa_phase]
102 name = uniform_angle
103
104 ; inclination prior
105 [prior-inclination]
106 name = sin_angle
107
108 ; polarization prior
109 [prior-polarization]
110 name = uniform_angle
111
112 ; sym. tidal deformability prior
113 [prior-tidal_ls]
114 name = uniform
115 min-tidal_ls = 0
116 max-tidal_ls = 2000
117
118 ; axion charge prior
119 [prior-axion_q]
120 name = uniform
121 min-axion_q = -0.5
122 max-axion_q = 0.5
123
124 ; axion charge difference prior
125 [prior-axion_dq]
126 name = uniform
127 min-axion_dq = -0.2
128 max-axion_dq = 0.2
```

Listing 11: *GW170817Ax.ini*, configuration file for axion case inference parameters and priors.

```
1 ; input strain data from LIGO detectors for GW170817 event
2 [data]
3 instruments = H1 L1
4 trigger-time = 1187008882.43
5
6 ; See the documentation at
7 ; http://pycbc.org/pycbc/latest/html/inference.html \\
8 ; #simulated-bbh-example
9 ; for details on the following settings:
10 analysis-start-time = -512
11 analysis-end-time = 32
12
13 ; psd settings
14 psd-estimation = median-mean
15 psd-start-time = -1800
16 psd-end-time = 128
17 psd-inverse-length = 8
18 psd-segment-length = 8
19 psd-segment-stride = 4
20
21 ; The frame files must be downloaded from GWOSC before running.
22 ; Adjust the file path as necessary.
23 frame-files = H1:data/H-H1_LOSC_CLN_16_V1-1187007040-2048.gwf \\
24 ; L1:data/L-L1_LOSC_CLN_16_V1-1187007040-2048.gwf
25 channel-name = H1:LOSC-STRAIN L1:LOSC-STRAIN
26 sample-rate = 2048
27
28 ; We'll use a high-pass filter so as not to get numerical errors \\
29 ; from the large
30 ; amplitude low frequency noise. Here we use 15 Hz, which is safely \\
31 ; below the
32 ; low frequency cutoff of our likelihood integral (20 Hz)
33 strain-high-pass = 15
34 ; The pad-data argument is for the high-pass filter: 8s are added to \\
35 ; the
36 ; beginning/end of the analysis/psd times when the data is loaded. \\
37 ; After the
38 ; high pass filter is applied, the additional time is discarded.
39 pad-data = 8
```

Listing 12: *data.ini*, configuration file for data input of GW170817 event.

```
1 ; Emcee sampler file
2 [sampler]
3 name = emcee
4 nwalkers = 100
5
6 ; length of run
7 effective-nsamples = 40000
8 checkpoint-interval = 1000
9 max-samples-per-chain = 40000
10
11 ; burn in finished, if one test passes
12 [sampler-burn_in]
13 burn-in-test = nacl | max_posterior
14
15 ; Sampling transforms
16 [sampling_params]
17 ; parameters OTL will be sampled in parametes OTR
18 mass1, mass2 : mchirp, q
19
20 [sampling_transforms-mchirp+q]
21 ; inputs mass1, mass2; outputs mchirp, q
22 name = mass1_mass2_to_mchirp_q
```

Listing 13: *emcee.ini*, configuration file for *emcee* sampler.

```
1 ; Emcee PT sampler file with 10 different temperatures
2 [sampler]
3 name = emcee_pt
4 nwalkers = 100
5 ntemps = 10
6
7 ; length of run
8 effective-nsamples = 40000
9 checkpoint-interval = 1000
10 max-samples-per-chain = 40000
11
12 ; burn in finished, if one test passes
13 [sampler-burn_in]
14 burn-in-test = nacl | max_posterior
15
16 ; Sampling transforms
17 [sampling_params]
18 ; parameters OTL will be sampled in parametes OTR
19 mass1, mass2 : mchirp, q
20
21 [sampling_transforms-mchirp+q]
22 ; inputs mass1, mass2; outputs mchirp, q
23 name = mass1_mass2_to_mchirp_q
```

Listing 14: *emceePt.ini*, configuration file for *emcee_pt* sampler.

References

1. K. S. Thorne. *Ligo and the Discovery of Gravitational Waves, III*. Nobel Lecture. regarding the Nobel Prize in Physics 2017 "for decisive contributions to the LIGO detector and the observation of gravitational waves". The Nobel Foundation, Dec. 2017. URL: <https://www.nobelprize.org/prizes/physics/2017/thorne/lecture/>.
2. *Introduction to LIGO & Gravitational Waves – Newton, Einstein and Gravitational Waves*. LIGO Scientific Collaboration. URL: <https://www.ligo.org/science/GW-GW.php> (visited on 12/11/2022).
3. B. W. Carroll and D. A. Ostlie. *An Introduction to Modern Astrophysics*. 2nd edition. Cambridge University Press, 2017. ISBN: 978-1-108-42216-1.
4. *GW170817: a binary neutron star merger*. Max-Planck-Gesellschaft, 2022. URL: <https://www.aei.mpg.de/151005/gw170817-a-binary-neutron-star-merger>.
5. *GW170817 – The first Observation of Gravitational-Waves from a binary neutron star inspiral*. LIGO Scientific Collaboration. URL: <https://www.ligo.org/detections/GW170817.php> (visited on 16/11/2022).
6. *LIGO, Virgo und KAGRA erhöhen ihren Punktestand auf 90*. Max-Planck-Gesellschaft, Nov. 2021. URL: <https://www.mpg.de/17799543/ligo-virgo-und-kagra-erhoehen-ihren-punktestand-auf-90>.
7. D. G. Y. P. Haensel A. Y. Potekhin, ed. *Neutron Stars 1 – Equation of State and Structure*. Vol. 326. Astrophysics and Space Science Library. Springer-Verlag New York, 2007. ISBN: 978-0-387-33543-8. DOI: [10.1007/978-0-387-47301-7](https://doi.org/10.1007/978-0-387-47301-7).
8. L. Rezzolla and O. Zanotti. *Relativistic Hydrodynamics*. Oxford University Press, 2013. ISBN: 978-0-19-852890-6.
9. K. S. Thorne et al. 'The theory of gravitational radiation: an introductory review.' In: *Les Houches Summer School on Gravitational Radiation*. Ed. by N. Deruelle and T. Piran. NATO Advanced Study Institute. 1983.
10. D. Baumann. *General Relativity*. lecture notes. Institute of Theoretical Physics, University of Amsterdam, Oct. 2019. URL: <http://cosmology.amsterdam/wp-content/uploads/2021/10/GR-Oct19.pdf>.
11. B. S. Sathyaprakash and B. F. Schutz. 'Physics, Astrophysics and Cosmology with Gravitational Waves'. In: *Living Reviews in Relativity* 12.1 (Mar. 2009). DOI: [10.12942/lrr-2009-2](https://doi.org/10.12942/lrr-2009-2). URL: <https://doi.org/10.12942/lrr-2009-2>.
12. L. Landau and E. Lifschitz. *klassische Feldtheorie*. Ed. by P. D. habil Hans-Georg Schöpf. 12. überarbeitete Auflage. Vol. 2. Lehrbuch der Theoretischen Physik. Verlag Europa-Lehrmittel, 1992. ISBN: 978-3-8085-5562-0.
13. M. Maggiore. *Gravitational Waves*. Vol. 1. Oxford University Press, 2008. ISBN: 978-0-19-857074-5.
14. A. Buonanno and B. Sathyaprakash. *Sources of Gravitational Waves: Theory and Observations*. Cambridge University Press, Sept. 2014. ISBN: 9781139583961. DOI: [10.1017/CB09781139583961.009](https://doi.org/10.1017/CB09781139583961.009).

15. L. Blanchet. ‘Gravitational Radiation from Post-Newtonian Sources and Inspiralling Compact Binaries’. In: *Living Reviews in Relativity* 9.1 (2006), p. 4. doi: [10.12942/lrr-2006-4](https://doi.org/10.12942/lrr-2006-4).
16. A. Buonanno et al. ‘Comparison of post-Newtonian templates for compact binary inspiral signals in gravitational-wave detectors’. In: *Phys. Rev. D* 80 (8 Aug. 2009), p. 084043. doi: [10.1103/PhysRevD.80.084043](https://doi.org/10.1103/PhysRevD.80.084043).
17. É. É. Flanagan and T. Hinderer. ‘Constraining neutron-star tidal Love numbers with gravitational-wave detectors’. In: *Phys. Rev. D* 77 (2 Jan. 2008), p. 021502. doi: [10.1103/PhysRevD.77.021502](https://doi.org/10.1103/PhysRevD.77.021502).
18. B. P. Abbott et al. ‘Model comparison from LIGO–Virgo data on GW170817’s binary components and consequences for the merger remnant’. In: *Classical and Quantum Gravity* 37.4 (Jan. 2020), p. 045006. doi: [10.1088/1361-6382/ab5f7c](https://doi.org/10.1088/1361-6382/ab5f7c).
19. J. Zhang et al. ‘First Constraints on Nuclear Coupling of Axionlike Particles from the Binary Neutron Star Gravitational Wave Event GW170817’. In: *Physical Review Letters* 127.16 (Oct. 2021). doi: [10.1103/physrevlett.127.161101](https://doi.org/10.1103/physrevlett.127.161101).
20. K. Yagi and N. Yunes. ‘Binary Love relations’. In: *Classical and Quantum Gravity* 33.13 (June 2016), 13LT01. doi: [10.1088/0264-9381/33/13/13LT01](https://doi.org/10.1088/0264-9381/33/13/13LT01).
21. A. Hook and J. Huang. ‘Probing axions with neutron star inspirals and other stellar processes’. In: *Journal of High Energy Physics* 2018.6 (7th June 2018), p. 36. doi: [10.1007/JHEP06\(2018\)036](https://doi.org/10.1007/JHEP06(2018)036).
22. L. Sagunski et al. ‘Neutron star mergers as a probe of modifications of general relativity with finite-range scalar forces’. In: *Physical Review D* 97.6 (Mar. 2018). doi: [10.1103/physrevd.97.064016](https://doi.org/10.1103/physrevd.97.064016).
23. J. Ellis et al. ‘Search for dark matter effects on gravitational signals from neutron star mergers’. In: *Physics Letters B* 781 (June 2018). doi: [10.1016/j.physletb.2018.04.048](https://doi.org/10.1016/j.physletb.2018.04.048).
24. T. P. Sotiriou and V. Faraoni. ‘ $f(R)$ theories of gravity’. In: *Reviews of Modern Physics* 82.1 (Mar. 2010), pp. 451–497. doi: [10.1103/revmodphys.82.451](https://doi.org/10.1103/revmodphys.82.451).
25. S. M. Carroll et al. ‘Is cosmic speed-up due to new gravitational physics?’ In: *Phys. Rev. D* 70 (4 Aug. 2004), p. 043528. doi: [10.1103/PhysRevD.70.043528](https://doi.org/10.1103/PhysRevD.70.043528).
26. S. S. Yazadjiev et al. ‘Non-perturbative and self-consistent models of neutron stars in R-squared gravity’. In: *Journal of Cosmology and Astroparticle Physics* 2014.06 (June 2014), p. 003. doi: [10.1088/1475-7516/2014/06/003](https://doi.org/10.1088/1475-7516/2014/06/003).
27. G. Alonso Alvarez. *Axions and other light dark matter candidates*. Universitätsbibliothek Heidelberg, 2020. doi: [10.11588/heidok.00028671](https://doi.org/10.11588/heidok.00028671).
28. E. Katz and M. D. Schwartz. ‘An eta primer: solving the U(1) problem with AdS/QCD’. In: *Journal of High Energy Physics* 2007.08 (Aug. 2007), p. 077. doi: [10.1088/1126-6708/2007/08/077](https://doi.org/10.1088/1126-6708/2007/08/077).
29. J. Preskill, M. B. Wise and F. Wilczek. ‘Cosmology of the invisible axion’. In: *Physics Letters B* 120.1 (1983), pp. 127–132. doi: [10.1016/0370-2693\(83\)90637-8](https://doi.org/10.1016/0370-2693(83)90637-8).
30. F. Chadha-Day, J. Ellis and D. J. E. Marsh. *Axion Dark Matter: What is it and Why Now?* 2021. doi: [10.48550/ARXIV.2105.01406](https://doi.org/10.48550/ARXIV.2105.01406).

31. R. Trotta. *Bayesian Methods in Cosmology*. 2017. DOI: [10.48550/ARXIV.1701.01467](https://doi.org/10.48550/ARXIV.1701.01467).
32. H. S. M. Coxeter. *Regular Polytopes*. third edition. Dover Publications, inc., 1973. ISBN: 9780486141589.
33. A. Nitz et al. *gwastro/pycbc*. release v2.0.2. PyCBC Development Team and the LIGO / Virgo Collaborations, Mar. 2022. DOI: [10.5281/zenodo.6912865](https://doi.org/10.5281/zenodo.6912865).
34. *PyCBC – Free and open software to study gravitational waves*. PyCBC Development Team and the LIGO / Virgo Collaborations. URL: <http://pycbc.org> (visited on 12/11/2022).
35. C. M. Biwer et al. ‘PyCBC Inference: A Python-based parameter estimation toolkit for compact binary coalescence signals’. In: *Publ. Astron. Soc. Pac.* 131.996 (2019), p. 024503. DOI: [10.1088/1538-3873/aaef0b](https://doi.org/10.1088/1538-3873/aaef0b). arXiv: [1807.10312](https://arxiv.org/abs/1807.10312) [astro-ph.IM].
36. D. Foreman-Mackey et al. ‘emcee: The MCMC Hammer’. In: *Publications of the Astronomical Society of the Pacific* 125.925 (Mar. 2013), p. 306. DOI: [10.1086/670067](https://doi.org/10.1086/670067). arXiv: [1202.3665](https://arxiv.org/abs/1202.3665) [astro-ph.IM].
37. W. D. Vousden, W. M. Farr and I. Mandel. ‘Dynamic temperature selection for parallel tempering in Markov chain Monte Carlo simulations’. In: *Monthly Notices of the Royal Astronomical Society* 455.2 (Nov. 2015), pp. 1919–1937. ISSN: 0035-8711. DOI: [10.1093/mnras/stv2422](https://doi.org/10.1093/mnras/stv2422). eprint: <https://academic.oup.com/mnras/article-pdf/455/2/1919/18514064/stv2422.pdf>.
38. *LIGO Algorithm Library - LALSuite*. free software (GPL). The LSC Algorithm Library Applications for gravitational wave data analysis. LIGO Scientific Collaboration, 2018. DOI: [10.7935/GT1W-FZ16](https://doi.org/10.7935/GT1W-FZ16).
39. D. Beazley et al. *SWIG-4.0*. free software (GPL). University of Chicago, 2021. URL: <https://www.swig.org>.
40. *LALSuite/axionEnv*. axionEnv branch of forked LALSuite repository. DMGW-Goethe, Oct. 2022. URL: <https://github.com/DMGW-Goethe/lalsuite/tree/axionEnv>.
41. *LALSuite/axionRemake*. axionRemake branch of forked PyCBC repository. DMGW-Goethe, Oct. 2022. URL: <https://github.com/DMGW-Goethe/pycbc/tree/axionRemake>.
42. *Slurm*. ITP IT Service Wiki page for the cluster usage with slurm. URL: <https://itp.uni-frankfurt.de/wiki-it/index.php/SLURM> (visited on 15/11/2019).
43. *FUCHS Cluster Usage*. Center for Scientific Computing Frankfurt, Oct. 2022. URL: <https://csc.uni-frankfurt.de/wiki/doku.php?id=public:usage:fuchs> (visited on 12/11/2022).
44. *Slurm – workload manager*. documentation regarding version 22.05. SchedMD, Oct. 2022. URL: <https://slurm.schedmd.com/documentation.html>.
45. *Storage and Backup*. ITP IT Service Wiki page for the data storage and file system structure. URL: https://itp.uni-frankfurt.de/wiki-it/index.php/Storage_and_Backup (visited on 10/03/2022).
46. A. Tridgell, P. Mackerras and W. Davison. *rsync - a fast, versatile, remote (and local) file-copying tool*. GNU General Public License. Nov. 2022. URL: <https://rsync.samba.org>.

47. B. P. Abbott et al. 'GW170817: Observation of Gravitational Waves from a Binary Neutron Star Inspiral'. In: *Physical Review Letters* 119.16 (Oct. 2017). doi: [10.1103/PhysRevLett.119.161101](https://doi.org/10.1103/PhysRevLett.119.161101).
48. B. P. Abbott et al. 'Gravitational Waves and Gamma-Rays from a Binary Neutron Star Merger: GW170817 and GRB 170817A'. In: *The Astrophysical Journal Letters* 848.2 (Oct. 2017), p. L13. doi: [10.3847/2041-8213/aa920c](https://doi.org/10.3847/2041-8213/aa920c).
49. R. Abbott et al. *Open data from the first and second observing runs of Advanced LIGO and Advanced Virgo*. Creative Commons Attribution 4.0 International License. LIGO Scientific Collaboration and Virgo Collaboration. doi: [10.7935/CA75-FM95](https://doi.org/10.7935/CA75-FM95).
50. R. Penrose. *The Road to Reality – A Complete Guide to the Laws of the Universe*. first vintage books edition. Vintage Books (Random House Inc.), 2007. ISBN: 978-0-679-77631-4.